Chapter 4

Anionic dioxidovanadium(V) complexes $[VO_2(L)]^-$ with (Z)-N'-(2-hydroxy-3-methoxybenzylidene) isonicotinic hydrazide as proligand and cation of imidazole units as ancillary ligands: Synthesis, characterization and *in-vitro* antidiabetic activity

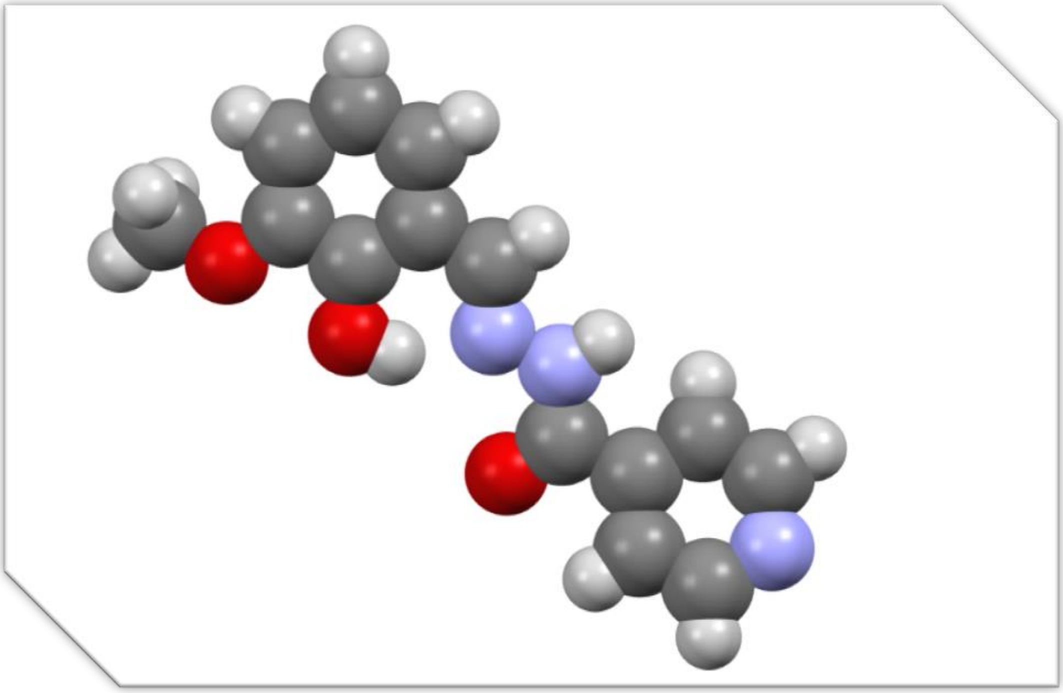

1 Introduction

Vanadium is a bio acceptable element and its complexes have attracted much attention owing to their involvement in various biological processes [1-6]. Vanadium complexes are used as homogeneous and heterogeneous catalysts in a number of reactions and in industrial processes [7-13]. Vanadium mimics the effect of insulin and has been exhibited its usefulness in treatment of type I and type II diabetes in various animal models along with limited human trials [14-18]. Diabetes is a lifestyle related disease and one of the most epidemic disease. This disease causes many severe secondary complications, including microangiopathy, kidney failure, cardiac abnormalities, diabetic retinopathy and eye disorders. Several factors, such as genetics, environment, eating habit, physiological states, hormones and stress are investigated to be associated with the development of disease like diabetes.

Schiff base complexes have been used as a versatile ligand in coordination chemistry. Schiff base hydrazones are versatile tridentate ligands and several types of V^{IV}-O, V^{V}-O and V^{V}-O_2 complexes have been synthesized [19-23]. Some of these complexes have been found as structural and functional mimics of antidiabetic [23-27]. However, very few studies have been explored the insulin mimicking effects of vanadium(IV/V) complexes with hydrazone ligands. Cations can have a significant impact on crystal architecture. Manifold effects can be established using organic cations, most frequently protonated cationic amines, pyridines and imidazoles. Organic cations can be varied through simple design and much functionality can be added. Columbic interactions are a main force for cation-anion adjustment in supramolecular structures [28]. Although, protonated organic cations can also act as multi-hydrogen bond donors and as well as acceptors and hence easily adjust the topologies *via* extra non-covalent interactions, charge assisted hydrogen bonds are stronger hydrogen bonds since ionic charge on a donor or acceptor increases the hydrogen bond strength [29-33].

The unique vanadium coordination environment with two oxido atoms of the VO_2^+ unit is suitable for building of non-covalent metal-organic compounds. These compounds can be designed by a covalent path using bridging ligands or by non-covalent path using hydrogen bonding and other weak interactions. The covalent path is based on strong covalent bonds associating the metal cations and organic ligands into potent polymeric compounds. In the non-covalent path much weaker forces, such as hydrogen bonding, C-H···π interaction and stacking (π···π) interactions etc. are used to construct metal-organic compounds. Among non-covalent interactions, hydrogen bonding is a strong building motif used in crystal engineering. By using a variety of hydrogen bonding donors-acceptors and their numbers can be varied through simple design. Thus, the use of hydrogen bonding is a prime choice for designing self-assembled compounds. Therefore, several coordination compounds can be designed into a desirable structure. These non-covalent interactions can even control the topology of metal-organic frameworks [34, 35] as well as the coordination geometry of compounds [36]. The above objective has been realized and therefore in this chapter, dioxidovanadium(V) complexes of ONO-Schiff base hydrazone has been synthesized using (H_2L) ligand with cations of imidazole or its derivatives namely, $[V(O)_2(L)]$ImH (**1**), $[V(O)_2(L)]$2-MeImH (**2**), $[V(O)_2(L)]$2-EthImH (**3**), $[V(O)_2(L)]$1-MeImH (**4**), $[V(O)_2(L)]$BezImH (**5**) and $[V(O)_2(L)]$2-MeBenzImH (**6**), where H_2L = Isonicotinicacid (2-hydroxy-3-methoxy-benzylidene)-hydrazide, ImH = Imidazole, 2-MeImH = 2-methylimidazole, 2-EthImH = 2-ethylimidazole, 1-MeImH = 1-methyl-1-imidazole, BenzImH = Benzimidazole and 2-MeBenzImH = 2-methylbenzimidazole (Chart 1).

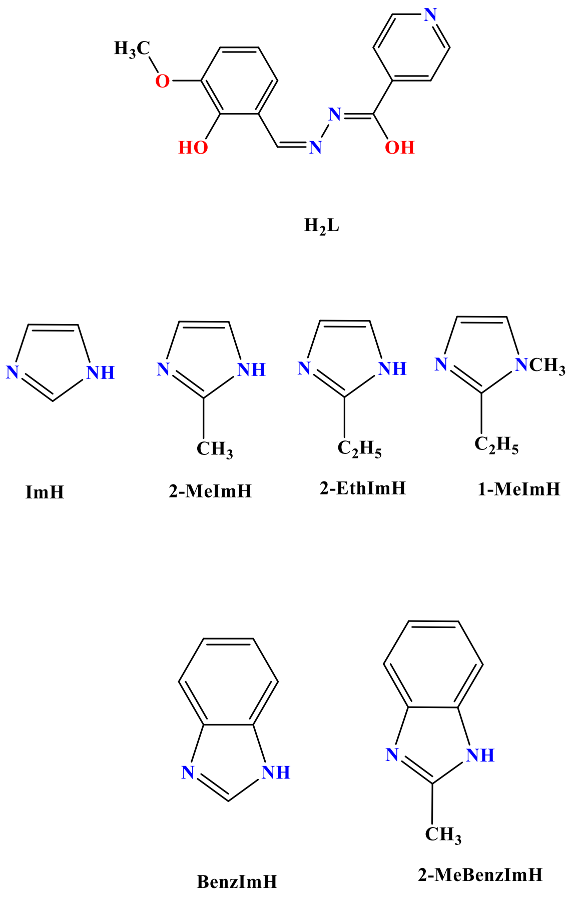

Chart 1 Structures of ligand and counter ions used.

These complexes are anionic with imidazolium ion as counter ion. These complexes have been characterized for their spectroscopic and redox properties. Moreover, *in-vitro* antidiabetic activity behaviours have also explored using α-glucosidase, β-glucosidase and α-amylase methods.

2 Experimental

2.1 Materials

All chemicals and solvents for syntheses were purchased commercially and were used without further purification. Vanadium pentaoxide was purchased from Across Organics. Spectroscopic grade solvents were used for spectral and electrochemical measurements.

2.2 Physical Measurements

Euro Vector EA3000 elemental analyzer was used to collect microanalysis (C, H and N) contents of compounds. FTIR spectra were recorded with a KBr pellet on a Bruker alpha FTIR-Spectrophotometer at 298 K. ^{1}H and ^{13}C NMR spectrum of ligand was recorded on a Bruker Advance III 400 MHz spectrometer. ESI Mass spectrometry was recorded on a XEVO G2-XS QTOF. Powder XRD was done by the Rigaku Desktop X-Ray diffractometer. Electronic spectra were recorded on a Shimadzu UV-1601 Spectrophotometer and corrected for the back ground resulting from the solvent absorption. Cyclic voltammetry (CV) experiments were carried out on a BAS-100 electrochemical analyzer in $3.0 \times 10^{-3}\mathrm{M}$ DMSO solution. A three-electrode setup was employed consisting of a glassy carbon working electrode, a platinum auxiliary electrode and Ag/AgCl as reference electrode and 0.1 M tetra butyl ammonium perchlorate (TBAP) was used as a supporting electrolyte. The ferrocenium/ferrocene couple was used to measure the redox potential. All measurements were done at 298K under a nitrogen atmosphere. Conductances of the complexes were measured on a type CM 82T Systronics direct-reading conductivity meter. A simultaneous TGA was performed using TG-DTA 6300 INCARP EXSTAR 6000 at a heating rate of 10 °C/min in the temperature range of 25-600°C with a nitrogen atmosphere maintained throughout the measurement. Single crystal X-ray diffraction data of ligand were collected at room temperature on X'calibur CCD area-detector diffractometer equipped with graphite monochromatic MoKα radiation (λ = 0.71073 Ǻ). The crystal used for data collection was of suitable dimensions. The unit cell parameters were determined by least-square refinements of all reflections in both cases. All the structures were solved by direct method and refined by full-matrix least-squares on F2. Data were corrected for Lorentz, polarization and multi-scan absorption correction [37]. All structures were solved by direct methods using SHELXS97 [38]. All non-hydrogen atoms were located in the best E-map. Full-matrix least-squares refinement was carried with SHELXL97 [38]. The geometry of the molecule has been calculated using the software PLATON [39] and PARST [40].

2.3 Computational Studies

All DFT system in was performed using the GAUSSIAN 09 program package [41] by the DFT/B3LYP method [42]. The input files of the vanadium(V) complexes were prepared with Gauss View 5.0.9 [43]. During optimization, the anion was ignored and only the cationic complexes were taken into account. The electronic excitations of the vanadium(V) complexes were made by using the time-dependent density functional theory (TD-DFT)/B3LYP method with a LANL2DZ basis set in the gas phase [44]. Vertical electronic excitations based on B3LYP optimized geometries were computed using the time-dependent density functional theory (TD-DFT) [45] in DMSO with a conductor-like polarizable continuum model (PCM) [46].

2.4 Antidiabetic activity

2.4.1 α-Glucosidase inhibition activity

The α-glucosidase inhibitory activity was investigated based on the reported in the literature, with a few modifications [47]. In brief, Rat-intestinal acetone powder was dissolved in 100 mL of saline water and sonicated properly at 4°C. After sonication, the suspension was centrifuged (3,000 rpm, 4°C, 30 minutes) and the resulting supernatant was used for the assay. A reaction mixture containing 50 µL of phosphate buffer (50 mM; pH 6.8), 50 µL of rat α-glucosidase and 50 µL sample of varying concentrations (100-800 µg/mL) was pre-incubated for 5 min at 37 °C and then 50 µL of 3 mM pNPG was added to the mixture as a substrate. After incubation at 37 °C for 30 min, enzymatic activity was quantified by measuring the absorbance at 405 nm in a microtiter plate reader (Bio-TEK, USA) and the values were compared with acarbose used as control. The percentage of α-glucosidase inhibitory activity (%) was calculated using equation (1).

$$\% \text{ inhibition} = [(A_C - A_S)/A_C] \times 100 \qquad \cdots (1)$$

where A_C and A_S are the absorbance changes of control and test samples respectively. The inhibitor concentration in the reaction mixture required to inhibit 50% of the enzyme is known as IC_{50}.

2.4.2 β-Glucosidase inhibition activity

The β-glucosidase inhibition study was carried out according to the reported methods [48] were used with some modification for the β-glucosidase inhibition activity. In brief, β-glucosidase of sweet almonds lyophilized powder for extra pure powder was dissolved in 100 mL assay buffer (pH 7.0) and sonicated properly at 4 °C. After sonication, the suspension was centrifuged (4,000 rpm, 4 °C, 30 minutes) and the resulting supernatant was used for the assay. Transfer 20 µL distilled water (H_2O) to two wells of a clear bottom 96-well plate. A reaction mixture containing 50 µL of buffer (50 mM; pH 6.8), 50 µL of p-Nitrophenyl-β-D-Glucopyranoside extra pure and 50 µL sample of varying concentrations (100-800 µg/mL) was pre-incubated for 20 min at 37 °C and then 50 µL of 3 mM pNPG was added to the mixture as a substrate. After incubation at 37 °C for 30 min, β-glucosidase enzymatic activity was determined by measuring the absorbance at 405 nm in a microtiter plate reader (Bio-TEK, USA). Acarbose was used as the control. The β-glucosidase inhibitory activity was calculated using the equation (1).

2.4.3 α-Amylase inhibition activity

Pancreatic α-amylase assay was adopted using the procedure described by Sudha et al. [49]. Briefly 50 µL of different dilutions of test compounds and 50 µL of 0.02 M sodium phosphate buffer (pH 6.9 with 0.006 M sodium chloride) containing α-amylase solution (0.5 mg/ mL) were incubated at 25°C for 10 min. After pre-incubation, 50 µL of 1% starch solution in 0.02 M sodium phosphate buffer (pH 6.9 with 0.006 M sodium chloride) was added to each tube. The reaction was incubated at 25°C for 10 min. The reaction was terminated by adding 100 µL of dinitro salicylic acid (DNS) colour reagent. Microplates were then incubated (85-90°C) for 10 min to develop colour and left to cool room temperature and diluted with 105 µL of distilled water. Enzymatic activity was quantified by measuring the absorbance at 540 nm in a microtiter plate reader (Bio-TEK, USA). Acarbose was used as standard and experiments were done in triplicates. The inhibition percentage was calculated using equation (1).

2.5 Synthesis of Schiff base (H_2L)

To the ethanolic solution (30 mL) of isonicotinic acid hydrazide (1.371 g, 10 mmol) an ethanolic solution (30 mL) of o-vanillin (1.521 g, 10 mmol) was added with 2-3 drops of glacial acetic acid as a catalyst and refluxed for 1 hrs. After refluxing 1 hrs the orange solution was cooled to room temperature and the resulting precipitate was filtered and washed with cold ethanol and dried in a $CaCl_2$ desiccator.

Yield: 87%. Anal. Calc. for $C_{14}H_{13}N_3O_3$ (271.27 g mol^{-1}) C, 61.98; H, 4.83; N, 15.49%. Found: C, 61.95; H, 4.85; N, 15.50%. FTIR bands (KBr, cm^{-1}): ν(O–H) 3440 s, ν(N–H) 998 (vs), ν(C=N) 1691(vs). ^{1}H NMR (DMSO-d_6 400 MHz) δ: 12.2 (s, 1H, Ar-OH), 10.8 (s, 1H, –NH), 8.4 (s, 1H, –CH=N), 9.4-6.7 (m, 7H, Ar-H), 3.82 (s, 3H, -OCH_3) ppm. ^{13}C NMR (DMSO-d_6 400 MHz) δ: 161 (C=O), 150 (C=N), 149 (C-OH), 150-114 (Ar-C), 56 (O-CH_3) ppm.

2.6. Synthesis of the dioxidovanadium(V) complexes

2.6.1. Synthesis of $[V(O)_2(L)]$ImH (1)

A methanolic solution (10 mL) of V_2O_5 (0.181 g, 1mmol) was added to the methanolic solution of H_2L (0.271 g, 1mmol) with stirring. To this reaction mixture (0.068 g, 1mmol) imidazole was added. The resulting reaction mixture was then refluxed for 3 hrs at 75 °C, under continuous stirring, cooled to room temperature and filtered. The filtrate was left for slow evaporation after one weak, radish brown powder of **1** separated. This was filtered, washed with cold methanol and dried in a calcium chloride desiccator.

Yield: 60%. Anal. Calc. for $C_{17}H_{16}N_5O_5V$ (421.29 g mol^{-1}). C, 48.47; H, 3.83; N, 16.62%. Found: C, 48.46; H, 3.81; N, 16.60%. FTIR bands (KBr, cm^{-1}): ν(C=N) 1633 (m), ν(C-O) 1291 (vs), ν(V=O) 942 (s), ν(V-O) 432, ν(V-N) 410 cm^{-1}. ESI Mass (m/z) = 422.50.

2.6.2 Synthesis of $[V(O)_2(L)]$2-MeImH (2)

The methanolic solution (10 mL) of H_2L (0.271 g, 1mmol) was prepared by heating and filtered. The methanolic solution (10 mL) of V_2O_5 (0.181 g, 1mmol) was added to the above solution with stirring. To this reaction mixture (0.082 g, 1mmol) 2-methylimidazole was added. The reaction mixture was then refluxed for 3 hrs at 75 °C, cooled to room temperature and filtered. The filtrate was left for slow evaporation, after 1-3 days, radish brown microcrystalline powder separated. This was filtered, washed with cold methanol and dried in a calcium chloride desiccator.

Yield: 62%. Anal. Calc. for $C_{18}H_{18}N_5O_5V$ (435.31 g mol^{-1}). C, 49.66; H, 4.17; N, 16.09%. Found: C, 49.65; H, 4.15; N, 16.06%. FTIR bands (KBr, cm^{-1}): ν(C=N) 1633 (m), ν(C-O) 1293 (vs), ν(V=O) 942 (s), ν(V-O) 433, ν(V-N) 411 cm^{-1}. ESI Mass (m/z) = 436.73.

2.6.3 Synthesis of [V(O)$_2$(L)]2-EthImH (3)

A solution of H_2L (0.271 g, 1 mmol) was prepared in 10 mL methanol by heating. A solution of V_2O_5 (0.181 g, 1mmol) in methanol (10 mL) was added to the above solution with stirring. To this reaction mixture (0.096 g, 1 mmol) 2-ethylimidazole was added. The resulting reaction mixture was then refluxed for 3 hrs at 75 °C, under continuous stirring, cooled to room temperature and filtered. The filtrate was left for slow evaporation, after 1-3 days, radish brown polycrystalline powder separated. This was filtered, washed with cold methanol and kept in a calcium chloride desiccator.

Yield: 67%. Anal. Calc. for $C_{19}H_{20}N_5O_5V$ (449.34 g mol^{-1}). C, 50.79; H, 4.49; N, 15.59%. Found: C, 50.76; H, 4 .48; N, 15.57%. FTIR bands (KBr, cm^{-1}): ν(C=N) 1633 (m), ν(C-O) 1299 (vs), ν(V=O) 942 (s), ν(V-O) 459, ν(V-N) 410 cm^{-1}. ESI Mass (m/z) = 450.25.

2.6.4 Synthesis of [V(O)$_2$(L)]1-MeImH (4)

A solution of H_2L (0.271 g, 1mmol) was prepared in 10 mL methanol by heating. To this solution, a solution of V_2O_5 (0.082 g, 1mmol) in methanol (10 mL) was added while stirring. To this reaction mixture (0.082 g, 1mmol) 1-methylimidazole was added. The resulting reaction mixture was then refluxed for 3 hrs at 75 °C, on cooling to room temperature, brown powder separated out. This was filtered, washed with cold methanol and dried in a calcium chloride desiccator.

Yield: 69%. Anal. Calc. for $C_{18}H_{18}N_5O_5V$ (435.29 g mol^{-1}). C, 49.66; H, 4.17; N, 16.09%. Found: C, 49.65; H, 4.16; N, 16.06%. FTIR bands (KBr, cm^{-1}): ν(C=N) 1633 (m), ν(C-O) 1299 (vs), ν(V=O) 941 (s), ν(V-O) 461, ν(V-N) 411 cm^{-1}. ESI Mass (m/z) = 435.50.

2.6.5. Synthesis of [V(O)$_2$(L)]BezImH (5)

This complex was synthesized as brown powder by following the method adopted in the synthesis of **1** using benzimidazole in place of imidazole.

Yield: 70%. Anal. Calc. for $C_{21}H_{18}N_5O_5V$ (471.35 g mol^{-1}). C, 53.51; H, 3.85; N, 14.86%. Found: C, 53.50; H, 3.87; N, 14.84%. FTIR bands (KBr, cm^{-1}): ν(C=N) 1633 (m), ν(C-O) 1299 (vs), ν(V=O) 1018 (s), ν(V-O) 459, ν(V-N) 410 cm^{-1}. ESI Mass (m/z) = 472.04.

2.6.6. Synthesis of [V(O)$_2$(L)]2-MeBenzImH (6)

This complex was isolated by adopting a similar method to that of **1** except that in place of imidazole 2-methylbenzimidazole was used.

Yield: 74%. Anal. Calc. for $C_{21}H_{18}N_5O_5V$ (485.37 g mol^{-1}). C, 53.51; H, 3.85; N, 14.86%. Found: C, 53.54; H, 3.84; N, 14.84%. FTIR bands (KBr, cm^{-1}): ν(C=N) 1633 (m), ν(C-O) 1299 (vs), ν(V=O) 941 (s), ν(V-O) 461, ν(V-N) 410 cm^{-1}. ESI Mass (m/z) = 485.69.

3 Results and discussion

The general method for the synthesis of ligand and complexes are shown in Scheme 1 and 2. The ligand (H_2L) was synthesized by mono condensation of the equimolar ratio of o-vanillin and isonicotinic hydrazide in ethanol. The complexes **1-6** were synthesized by the reaction of V_2O_5, H_2L and imidazoles or its derivatives in a 1:1:1 molar ratio in methanol under reflux for 1 hrs. The brown-colored polycrystalline powder was obtained. Unfortunately, these complexes could not be crystallized in spite of our several best efforts. These complexes are insoluble in common organic solvents such as dichloromethane, chloroform, benzene, hexane and ether, etc. while soluble in polar organic solvents, such as acetonitrile and dimethyl sulphoxide. These are stable in the solid-state. The isolated complexes with their compositions are shown in Scheme 2.

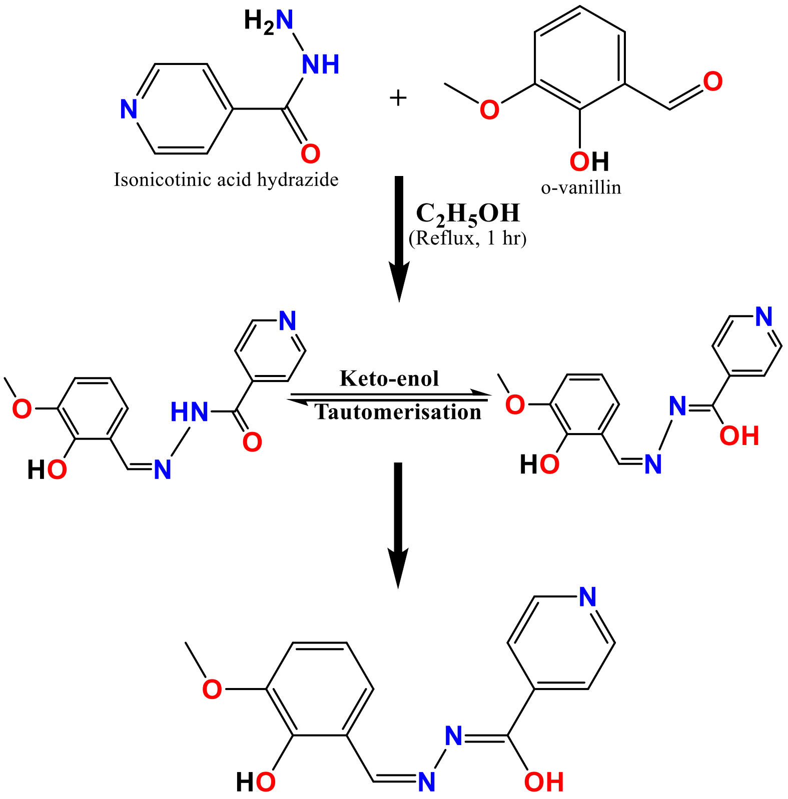

H_2L = Isonicotinic acid (2-hydroxy-3-methoxy-benzylidene)-hydrazide

Scheme 1 Synthesis and keto-enol tautomerization of ligand **(H_2L).**

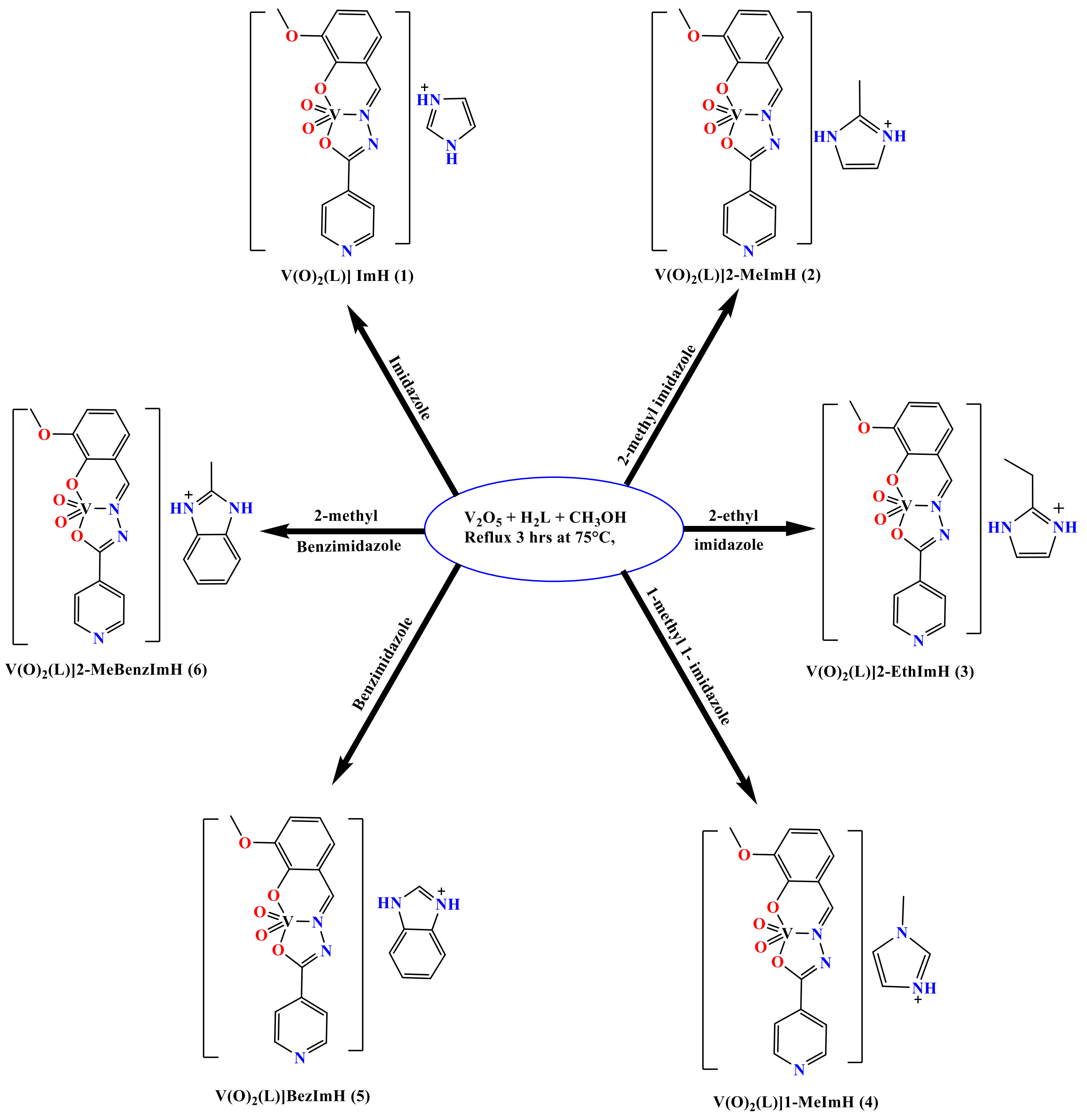

Scheme 2 Synthetic route of dioxidovanadium(V) complexes **1-6**.

3.1 NMR Spectra of Ligand

The ^{1}H and ^{13}C NMR spectra of Schiff base was measured in DMSO-d$_6$. The ^{1}H spectrum is shown in Fig. 1. The NMR data for the Schiff base are completely consistent with the formulation shown in Scheme 1. The ^{1}H NMR spectrum of Schiff base shows peaks at δ = 12.2 and 10.7 ppm due to phenolic proton (s, 1H, OH) and secondary NH proton (s, 1H, NH) of isonicotinic moiety of the ligand. This suggests that the Schiff base exists in the ketonic form [50-53]. The peak corresponding to azomethine proton (s, 1H, CH=N) appears at δ = 8.4 ppm. The peaks at δ = 8.8 and 8.7 ppm are due to adjacent C atoms of N in the pyridyl ring (^{1}H, N-CH, ^{1}H, N=CH). The peak of O-CH_3 moiety of ligand appears at δ = 3.8 (s, 3H, O-CH_3). The aromatic protons that appear in the expected region of 7.2-6.8 ppm are related to H atoms of benzene and pyridyl rings (d, t, 4H). Similarly, ^{13}C NMR spectrum of Schiff base measured in DMSO-d_6. ^{13}C NMR displays a peak at δ = 150.1 ppm due to C atom of a benzene ring attached to phenoxy group (s, 1C, C-OH). Carbon atom where a hydroxyl group of isonicotinic acid attached yielded δ = 150 ppm. The C atom of the carbonyl and azomethine moiety of Schiff base is reflected at δ = 161 and 150 ppm. The methoxy group containing the C atom of the benzene ring shows a peak as δ = 149 ppm. The peak corresponding to the C atom adjacent to the pyridine N atom appears at δ = 147 and 148 ppm. The remaining peak observed in the range 140-114 ppm in the NMR spectrum is due to C atoms (s, 7 C). The C atom of the methoxy group of H_2L shows the peak at δ = 56 ppm [54]. ^{13}C NMR spectrum is shown in Fig. 2.

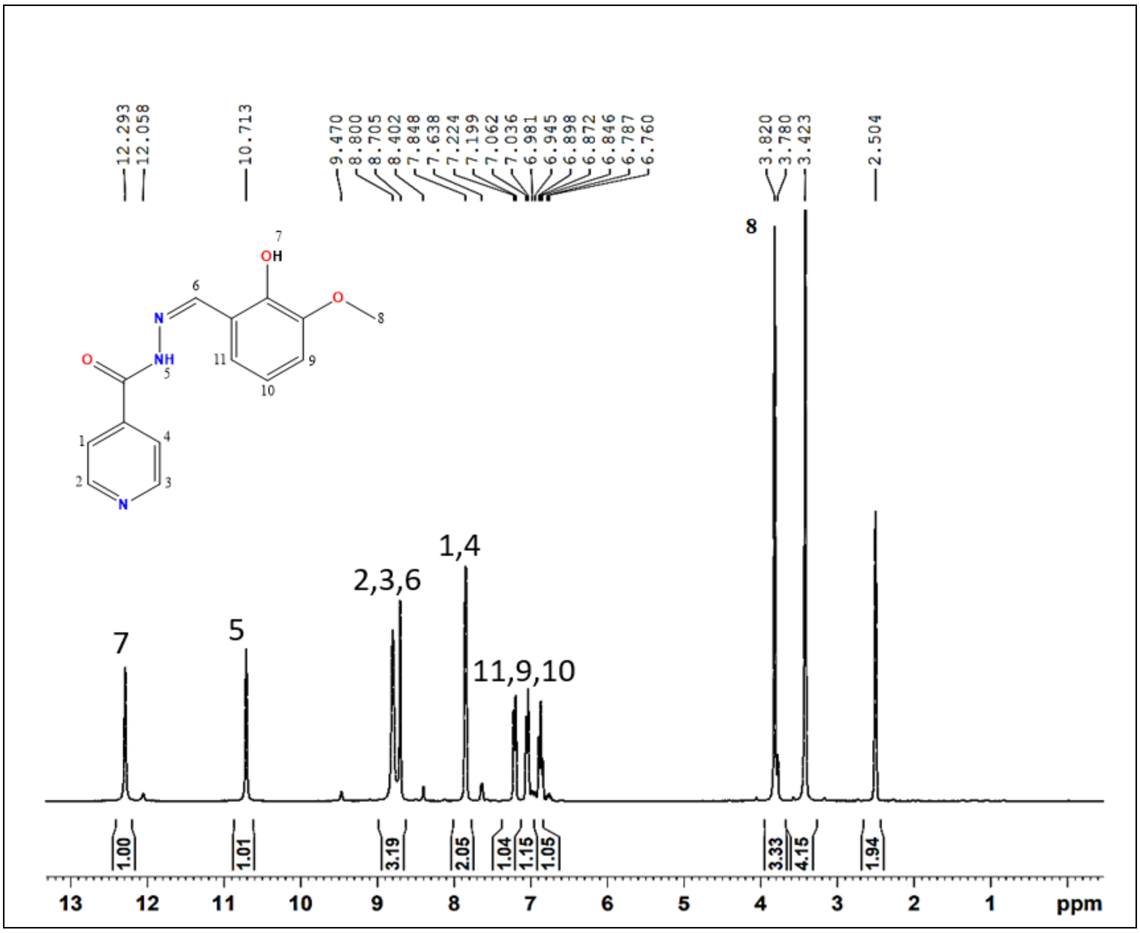

Fig. 1. ^{1}H NMR of H_2L ligand.

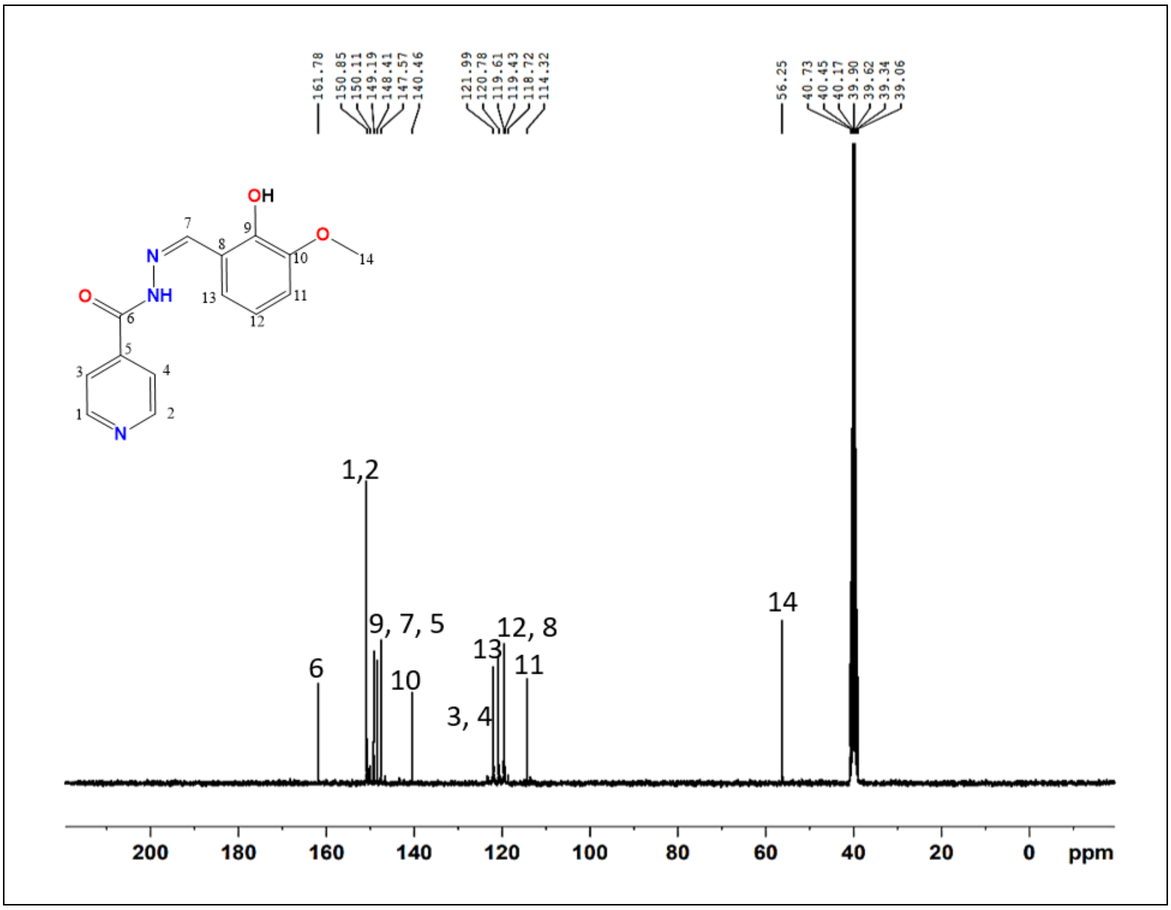

Fig. 2. ^{13}C NMR of H_2L ligand.

3.2 Mass spectral studies

The mass spectra of complexes were in good agreement with the proposed structures. The mass of all complexes was done in positive mode only. The mass of all complexes was obtained in between the range of $[M+1]^+$ to $[M+3]^+$. The mass spectrum of **1** shows a molecular ion (m/z) peak at $[M+1]^+$ 422.50, which proves the formation of the complex. The ESI-mass of all complexes is in good agreement with the molecular mass of complexes **1-6.** The mass of complexes is shown in Fig. 3-8.

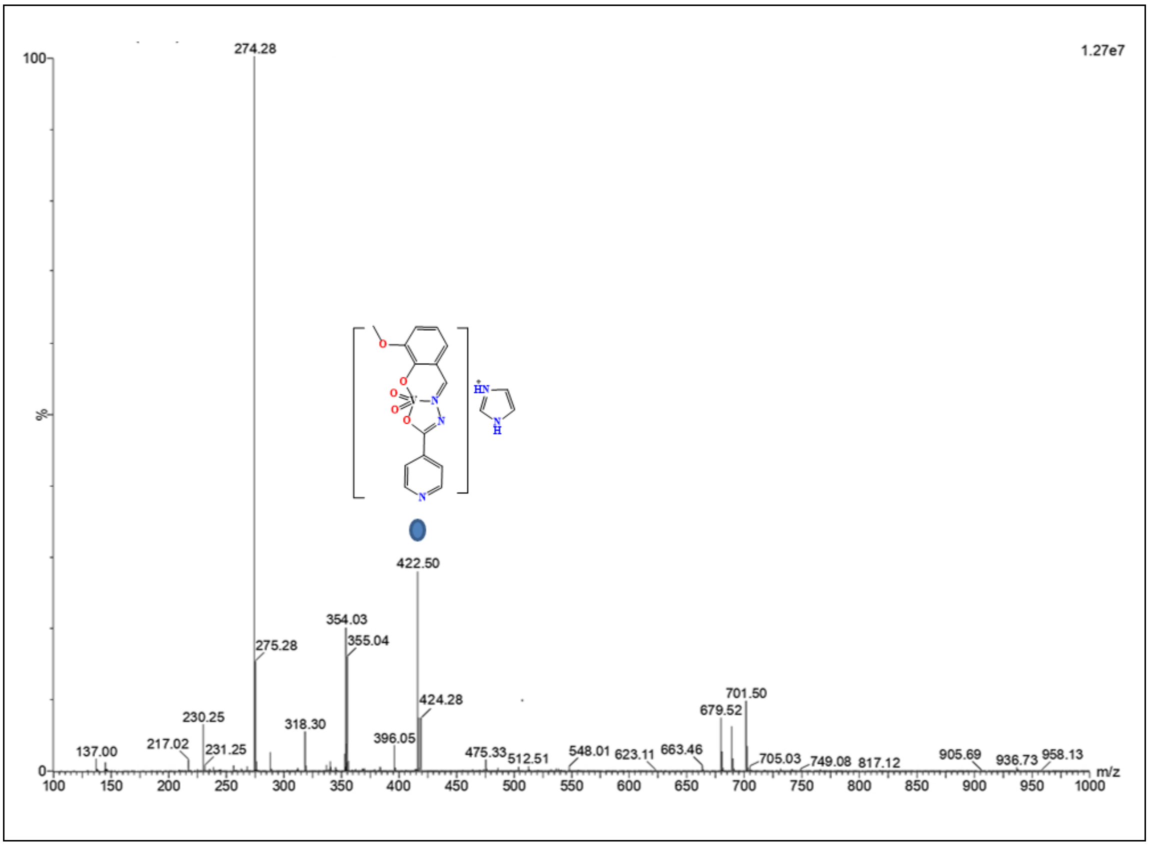

Fig. 3. Mass spectrum of complex **1**.

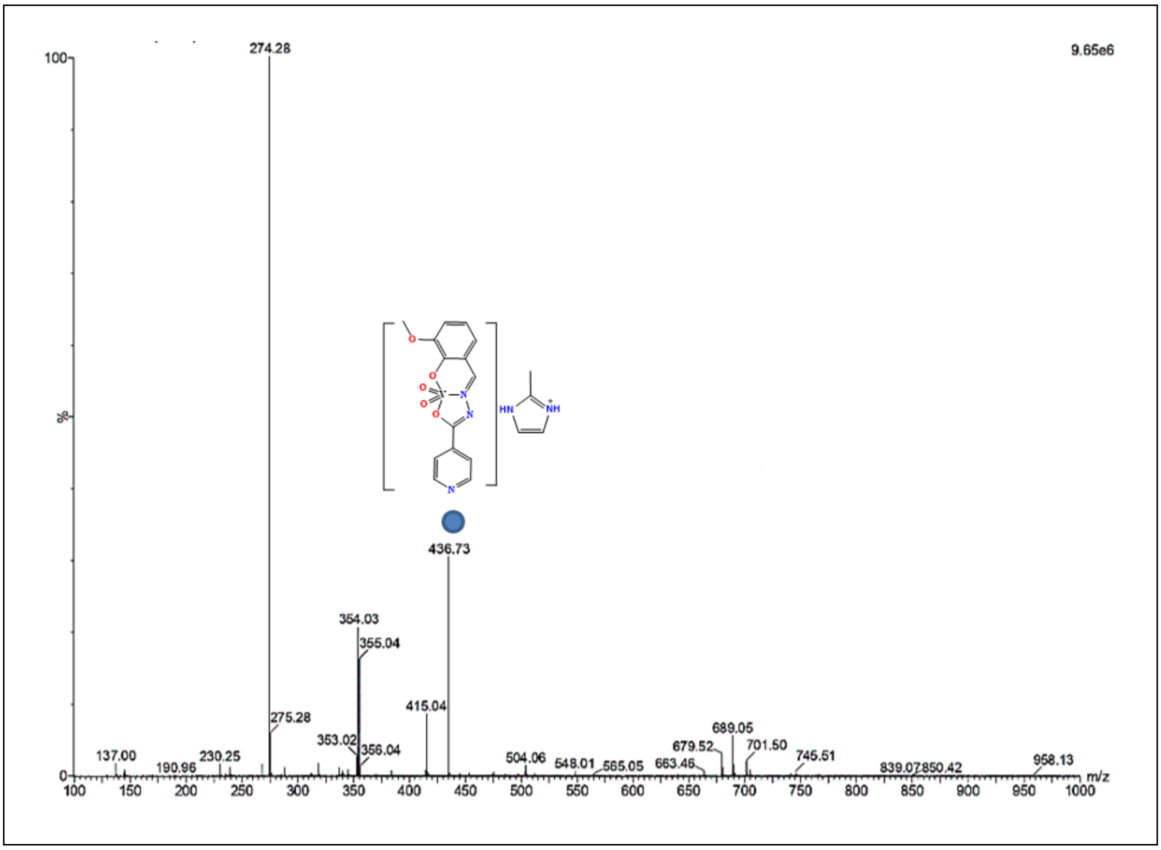

Fig. 4. Mass spectrum of complex **2**.

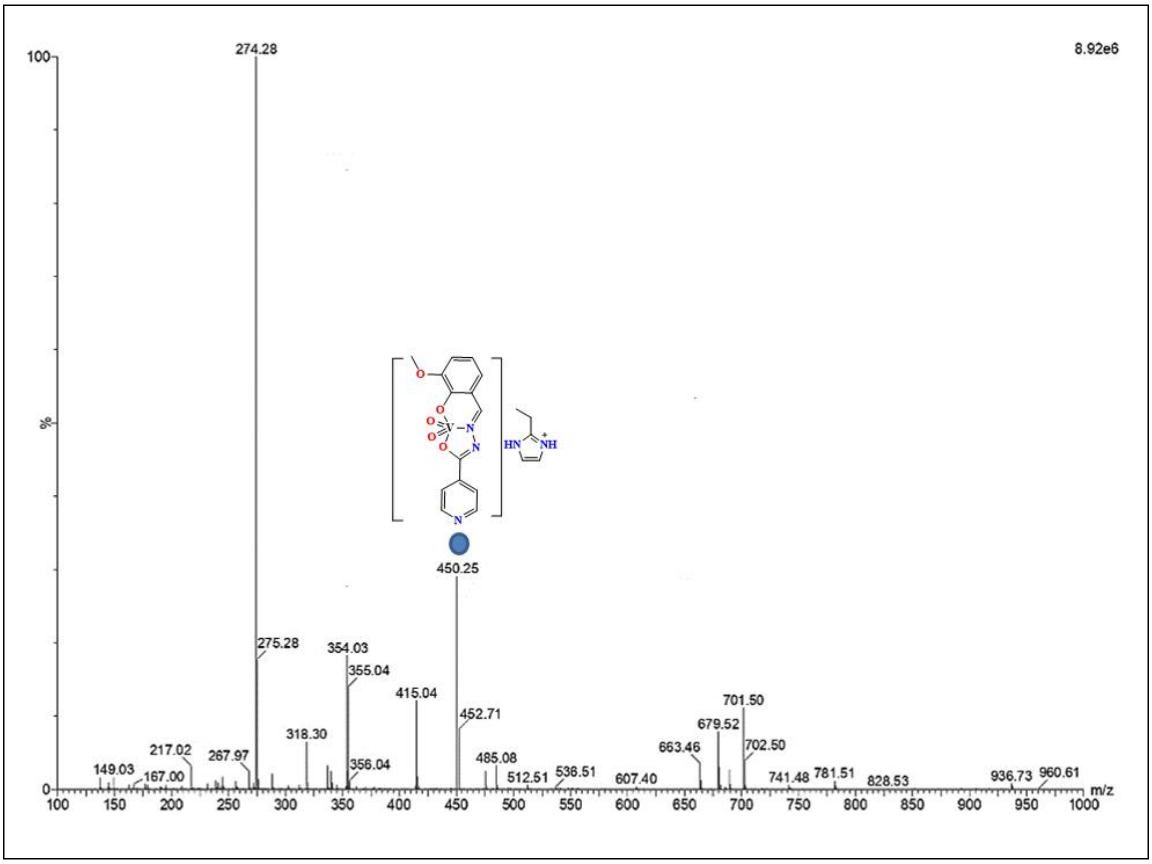

Fig. 5. Mass spectrum of complex **3**.

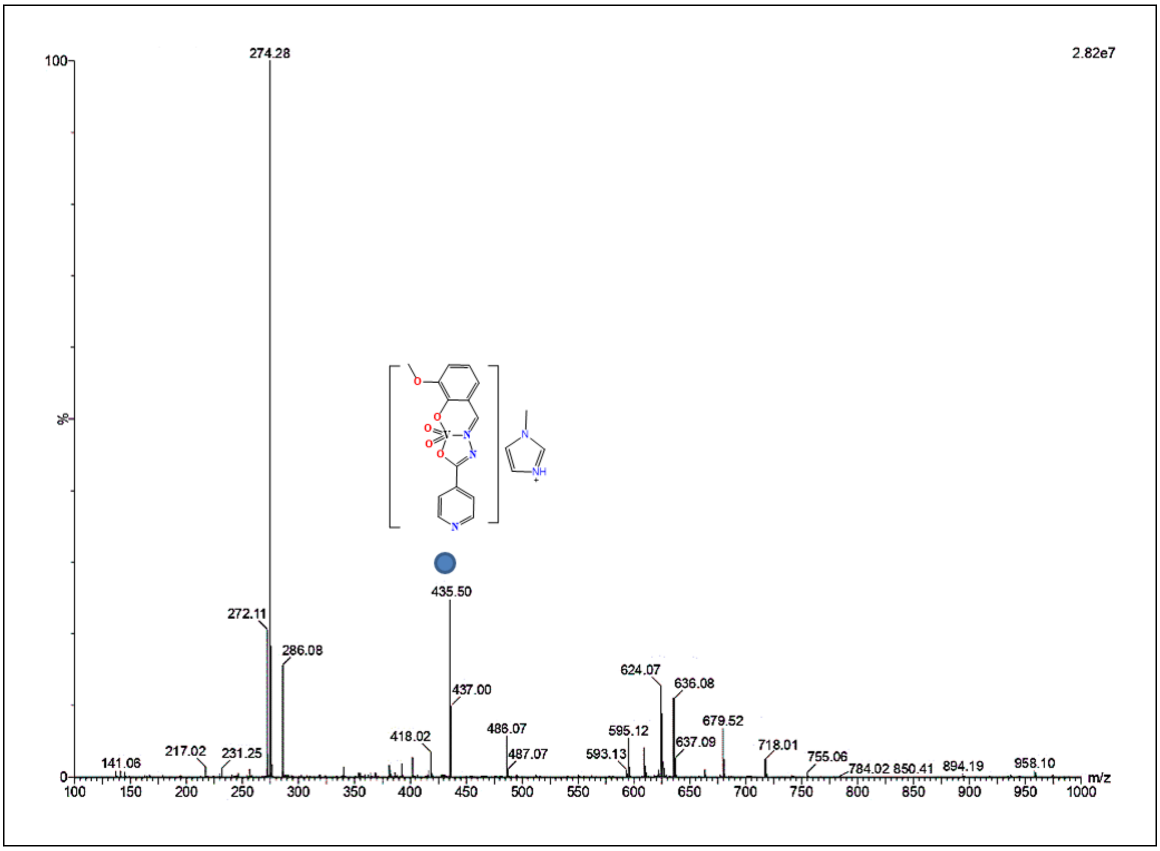

Fig. 6. Mass spectrum of complex **4**.

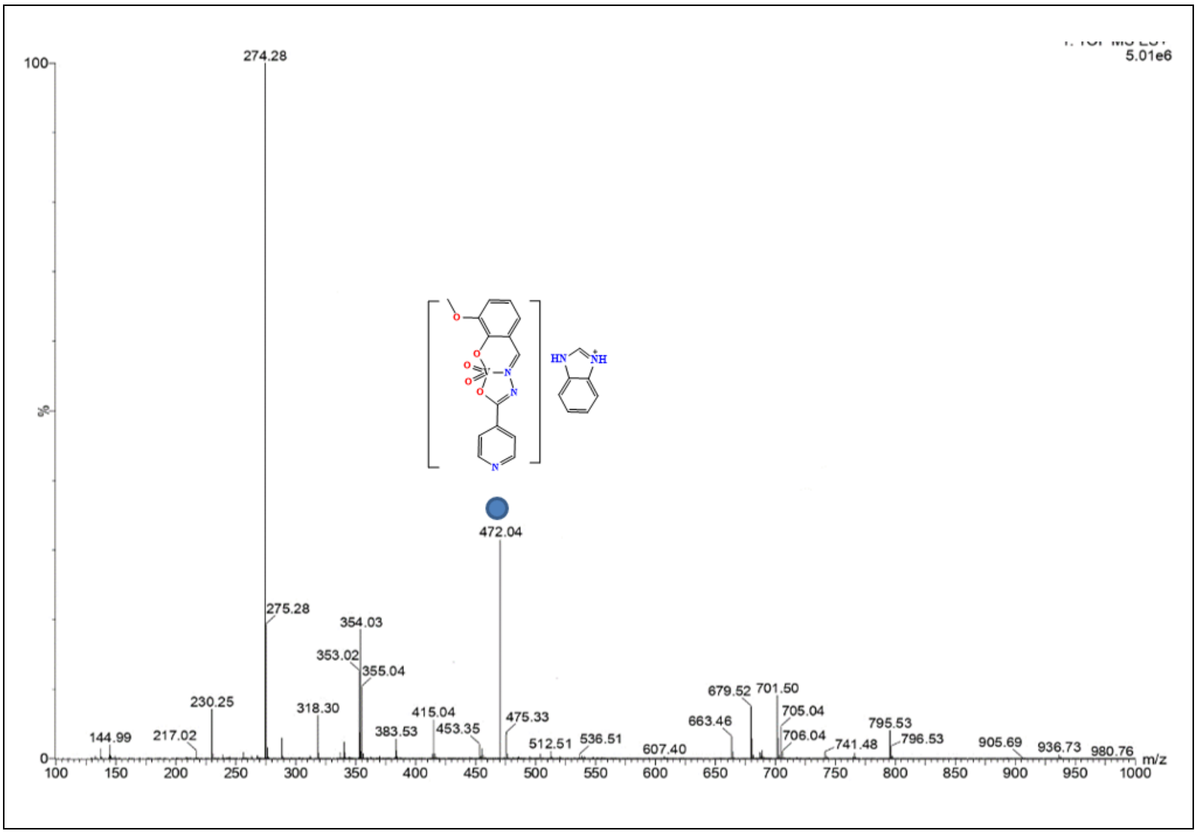

Fig. 7. Mass spectrum of complex **5**.

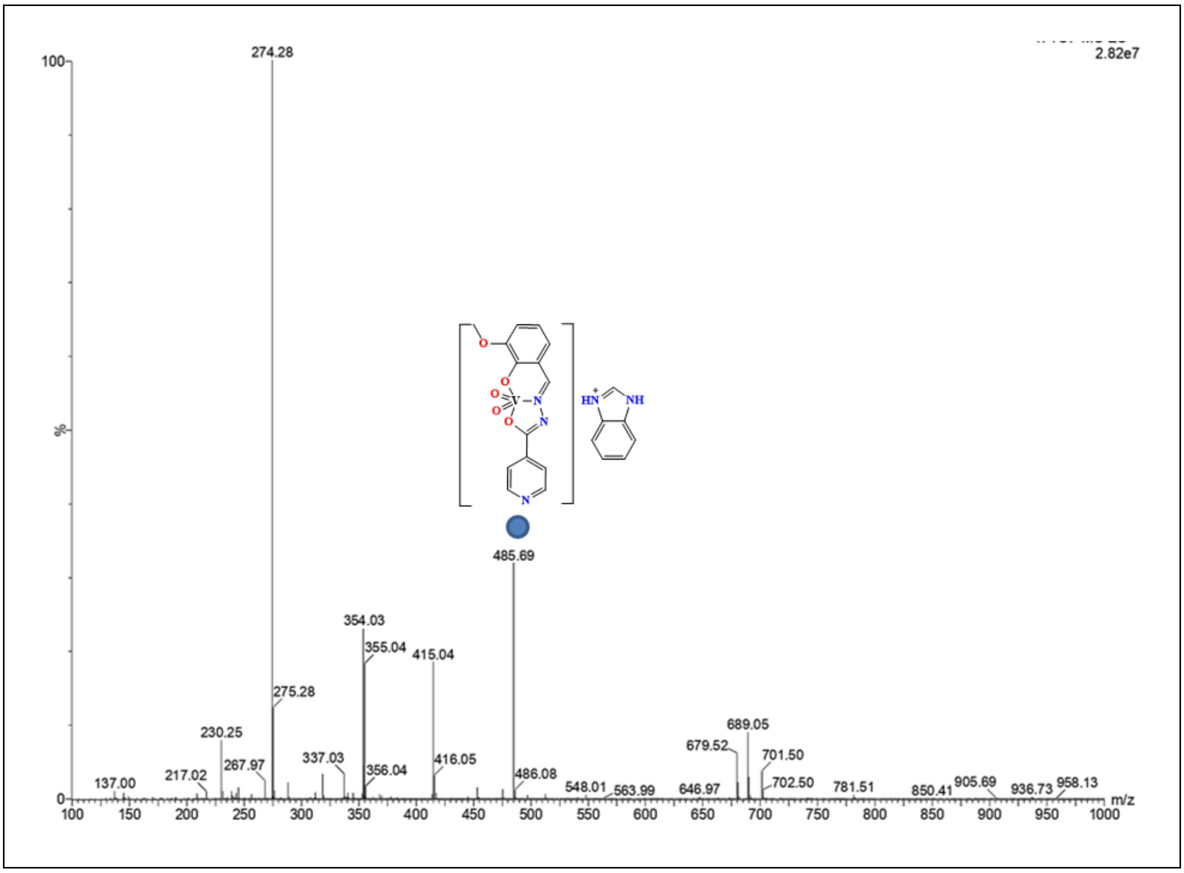

Fig. 8. Mass spectrum of complex **6**.

3.3 Crystal Structure of Ligand (H_2L)

The crystal image and crystal structure of the free ligand (H_2L) is shown in Fig. 9a and b. Crystal data and structure refinement for ligand are shown in Table 1 The single-crystal structure displays that the enolic proton is transferred to the imine nitrogen and hence ligand is in keto-imine form. The phenolic proton forms intramolecular hydrogen bonding with imine nitrogen and thus a six-atom pocket, $R_1^1(6)$ is generated. The bond length of C1-O1 and C9-O2 have the values 1.2186(12) Å and 1.3496(11) Å respectively. Both bond lengths are almost similar and are within the limit of a C-O single bond Table 2 [55]. Pyridine nitrogen is a bi-furcated donor atom for generating intermolecular hydrogen bonding. Other intermolecular hydrogen bonding is due to methoxy oxygen and proton of C-H shown in Table 3 Fig. 10. The packing of the ligand is dominated by intramolecular and intermolecular hydrogen bonds. Two molecules are well connected by intermolecular hydrogen bindings Fig. 11.

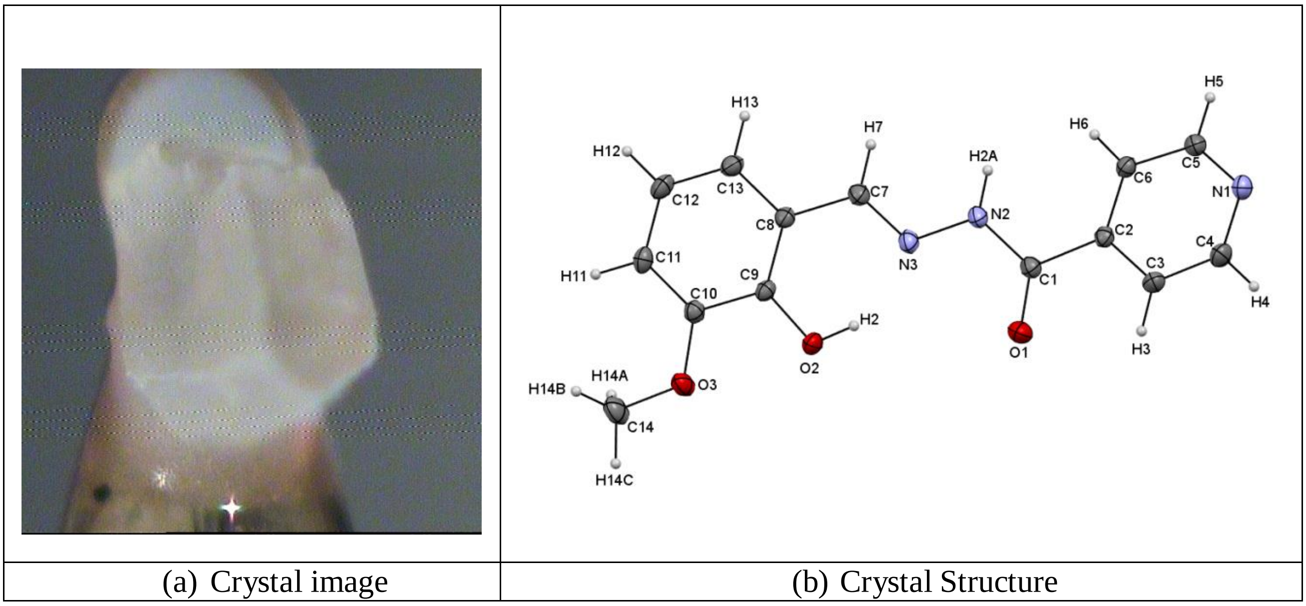

(a) Crystal image

(b) Crystal Structure

Fig. 9. (a) Crystal image and **(b)** Crystal structure of ligand **H_2L**.

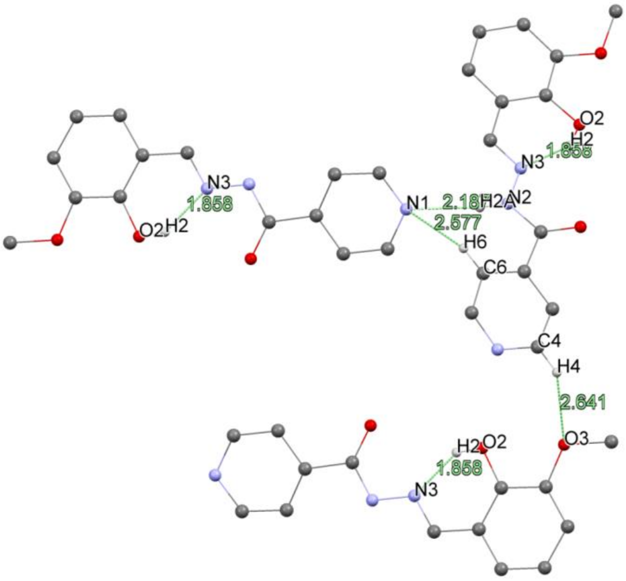

Fig. 10. H-bondings in ligand molecule $\mathbf{H_2L}$.

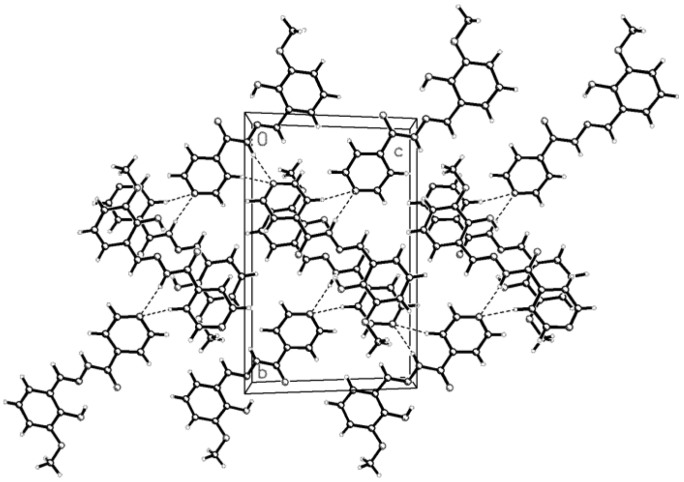

Fig. 11. Crystal packing diagram of the ligand $\mathbf{H_2L}$.

Table 1 Crystal data and structure refinement for $\mathbf{H_2L}$.

	$\mathbf{H_2L}$
Empirical formula	$C_{14}H_{13}N_3O_3$
Formula weight	271.27
Temperature/K	173(2)
Crystal system	Monoclinic
Space group	$P2_1/n$
a/Å	7.5662(3)
b/Å	16.2532(5)
c/Å	10.7888(4)
α/°	90

β/°	109.831(4)
γ/°	90
Volume/Å^3	1248.07(8)
Z	4
ρ_{calc}g/cm^3	1.444
μ/mm^{-1}	0.104
F(000)	568.0
Crystal size/mm^3	0.38 × 0.32 × 0.26
Radiation	MoKα (λ = 0.71073)
2Θ range for data collection/°	7.612 to 65.224
Index ranges	$-10 \leq h \leq 11$, $-21 \leq k \leq 24$, $-15 \leq l \leq 13$
Reflections collected	15041
Independent reflections	4225 [R_{int} = 0.0227, R_{sigma} = 0.0224]
Data/restraints/parameters	4225/0/183
Goodness-of-fit on F^2	1.048
Final R indexes [I>=2σ (I)]	R_1 = 0.0425, wR_2 = 0.1151
Final R indexes [all data]	R_1 = 0.0541, wR_2 = 0.1241
Largest diff. peak/hole / e Å^{-3}	0.37/-0.21

Table 2 Bond Length (Å) and Bond Angle (°) of **H_2L**.

H_2L			
Bond length			
O1-C1	1.2186(12)	N1-C4	1.3395(13)
O2-C9	1.3496(11)	N1-C5	1.3378(12)
O3-C10	1.3651(12)	N2-N3	1.3705(11)
O3-C14	1.4260(12)	N2-C1	1.3633(12)
N3-C7	1.2842(12)		
Bond angle			
C10-O3-C14	116.87(8)	N2-C1-C2	114.94(8)
C5-N1-C4	116.78(8)	N3-C7-C8	120.42(9)
C1-N2-N3	117.54(8)	C9-C8-C7	121.05(8)
C7-N3-N2	117.85(8)	O2-C9-C8	123.07(8)
O1-C1-N2	123.46(9)	O2-C9-C10	117.09(8)
O1-C1-C2	121.58(9)	C8-C9-C10	119.82(8)

Table 3 Hydrogen bond parameters (Å/°) in the crystal structure of **H_2L**.

D-H···A	d(D-H)	d(H-A)	d(D-A)	D-H-A/°	Symmetry
O2H2N3	0.84	1.86	2.5938(11)	145.4	
N2H2AN1[1]	0.88	2.19	3.0479(12)	166.0	[1]-1/2+X,3/2-Y,-1/2+Z
C4H4O3[2]	0.95	2.64	3.3568(13)	132.5	[2]1/2-X,1/2+Y,3/2-Z
C6H6N1[1]	0.95	2.58	3.3609(12)	140.0	

3.4 Powder X-ray diffraction

As single crystals of complexes **1-6** could not be obtained after several affords, therefore, polycrystalline X-ray diffraction patterns were collected for present complexes. The d-spacing and calculated h, K and L values at different 2θ are shown in Table 4. However, several spectroscopic techniques could be used with good effect to characterizing these metal complexes. The X-ray diffraction (XRD) patterns are shown in Fig. 12-17. These complexes show peaks at 2θ = 0-80° exhibiting their crystalline nature. The distribution of the peaks in XRD patterns revealed an excellent crystalline for the morphology of all complexes [56, 57]. The extracted few data from the XRD pattern provide the single physic nature of complexes.

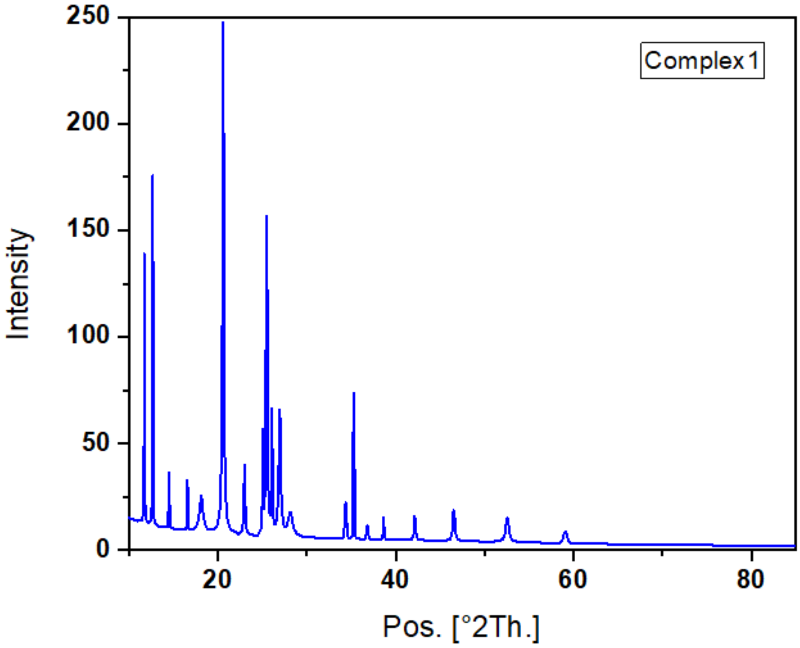

Fig. 12. Powder XRD pattern for complex **1**.

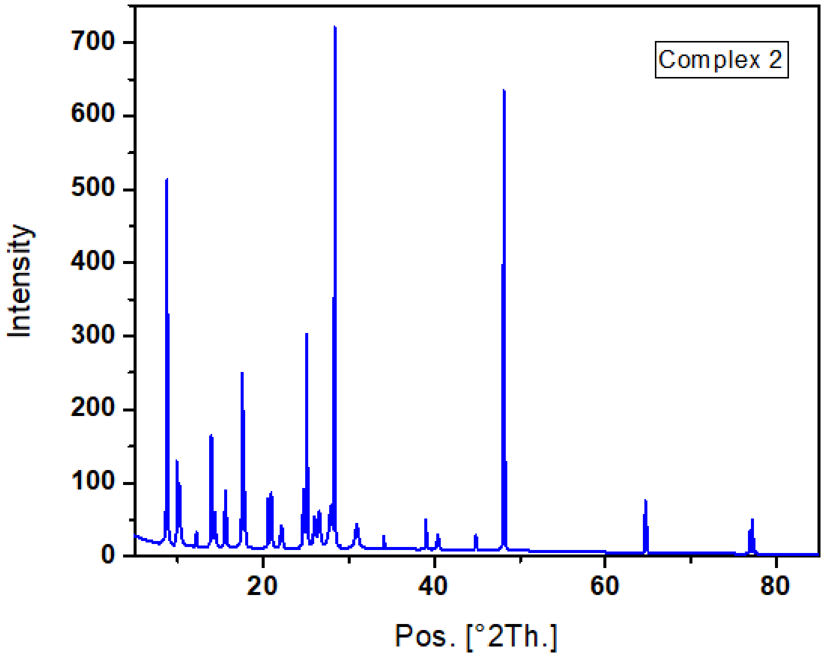

Fig. 13. Powder XRD pattern for complex **2**.

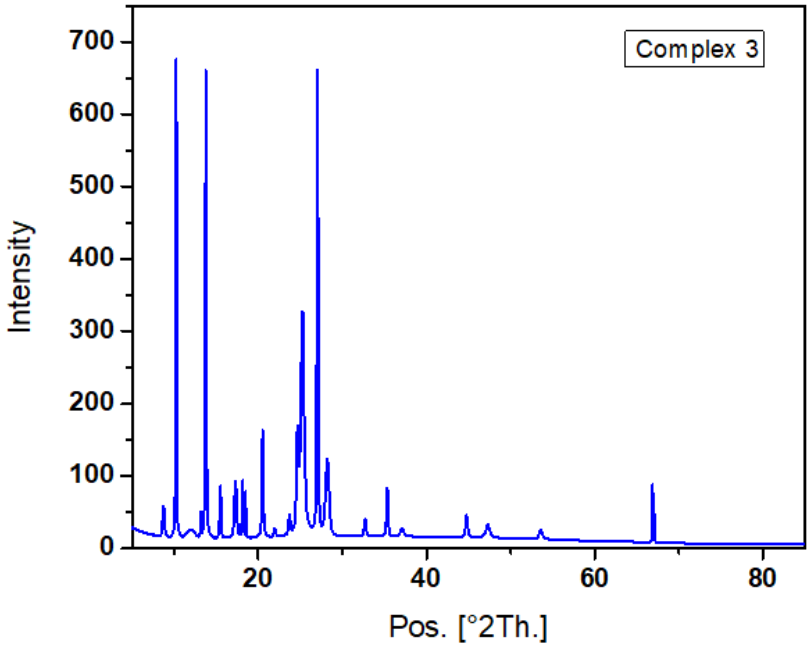

Fig. 14. Powder XRD pattern for complex **3**.

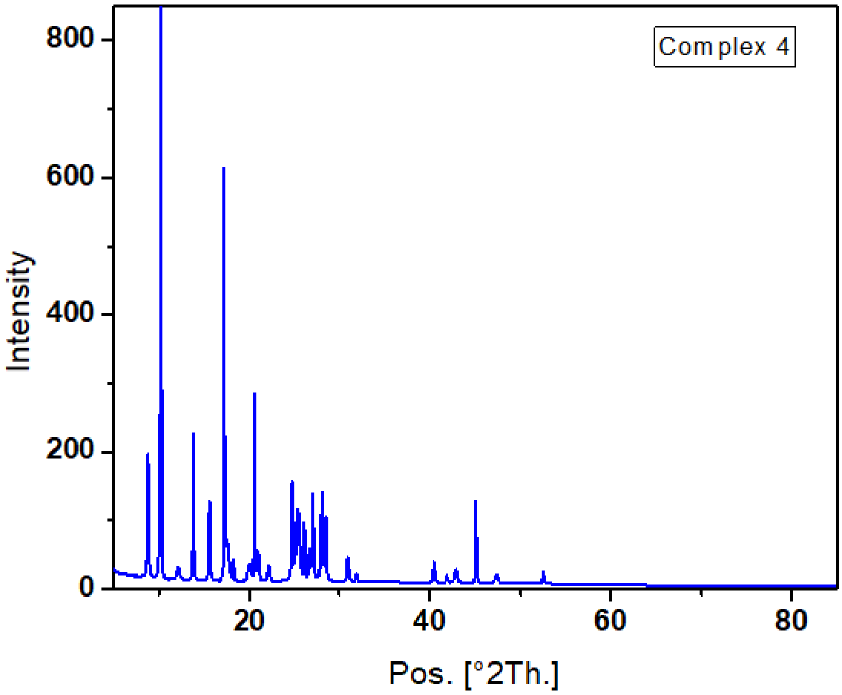

Fig. 15. Powder XRD pattern for complex **4**.

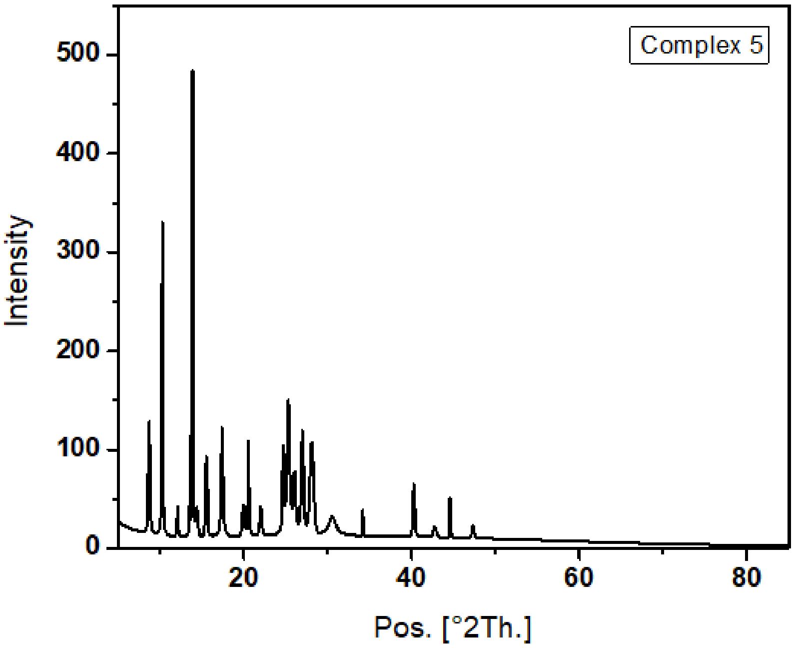

Fig. 16. Powder XRD pattern for complex **5**.

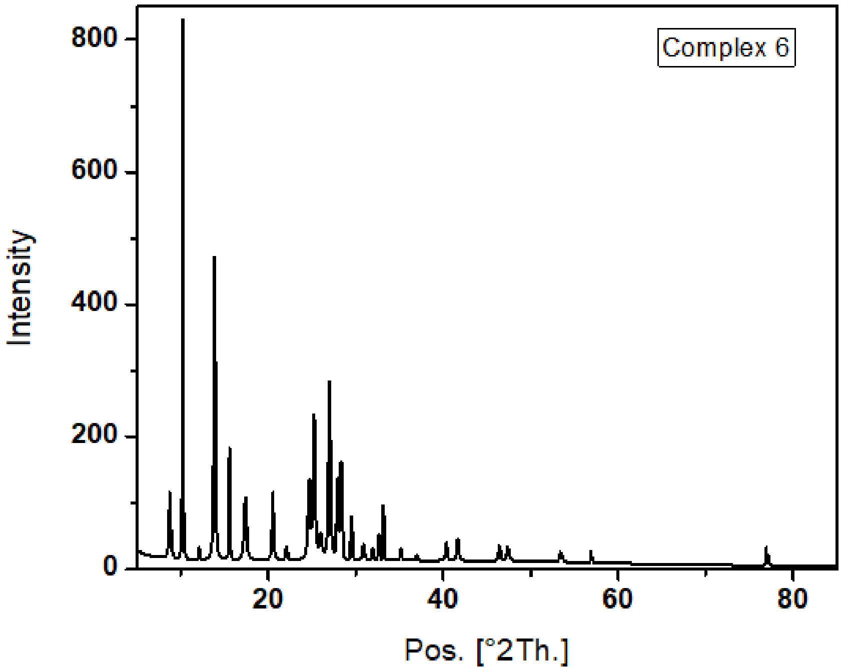

Fig. 17. Powder XRD pattern for complex **6**.

Table 4 X-ray diffraction data of the complexes **1-6**.

Observed 2θ	**Calculated 2θ**	***d* spacing**	***H***	***K***	***L***	**Difference 2θ**
1						
18.18	18.11	4.895	1	1	1	0.07
26.12	26.06	3.415	1	0	6	0.06
26.92	26.92	3.308	0	0	7	0.00
34.49	34.43	2.608	2	2	1	0.06
46.64	46.61	1.951	4	0	0	0.03
52.53	52.49	1.741	4	1	1	0.04
2						
12.03	11.99	7.376	1	0	0	0.04
15.50	15.47	5.722	0	0	4	0.03
18.16	18.12	4.891	1	1	1	0.04
20.50	20.48	4.331	1	1	3	0.02
35.32	35.29	2.541	2	2	1	0.03
37.11	37.07	2.423	3	0	0	0.04
3						
12.19	12.16	7.270	1	0	0	0.03
17.89	17.86	4.960	1	1	1	0.03
24.71	24.70	3.600	1	1	5	0.01

26.58	26.54	3.356	0	0	7	0.04
40.44	40.41	2.230	2	2	6	0.03
54.79	54.77	1.234	4	1	1	0.02
4						
18.26	18.22	4.864	1	1	1	0.04
20.96	20.94	4.239	1	1	3	0.02
26.08	26.02	3.420	1	0	6	0.06
26.64	26.61	3.347	0	0	7	0.03
31.85	31.83	2.809	1	1	7	0.02
52.48	52.46	1.742	4	1	1	0.02
5						
15.53	15.53	15.53	15.53	15.53	15.53	15.53
20.55	20.55	20.55	20.55	20.55	20.55	20.55
26.07	26.07	26.07	26.07	26.07	26.07	26.07
26.98	26.98	26.98	26.98	26.98	26.98	26.98
34.19	34.19	34.19	34.19	34.19	34.19	34.19
42.76	42.76	42.76	42.76	42.76	42.76	42.76
6						
15.56	15.56	15.56	15.56	15.56	15.56	15.56
22.16	22.16	22.16	22.16	22.16	22.16	22.16
25.99	25.99	25.99	25.99	25.99	25.99	25.99
31.91	31.91	31.91	31.91	31.91	31.91	31.91
40.43	40.43	40.43	40.43	40.43	40.43	40.43
53.55	53.55	53.55	53.55	53.55	53.55	53.55

3.5 Molar conductance

The molar conductance for complexes **1-6** measured in DMSO solution (1×10^{-3} M). The observed values are in 65-73 $\Omega^{-1}\mathrm{cm}^2\mathrm{mol}^{-1}$ range. The molar conductance value of complexes is given in Table 5. Although these values are slightly less than the molar conductance values for a monoanionic nature (1:1:1) [58]. This could be due to the low mobility because of the large size of their ions in the solution. Therefore, these complexes show less molar conductance.

Table 5 Molar conductance of complexes **1-6**.

Complex	Molar conductance Λ (Ω^{-1} cm^2 mol^{-1})
1	73.52
2	70.24
3	68.05
4	71.24
5	65.04
6	66.02

3.6 FTIR spectral study

The FTIR spectral data of ligand and complexes are given in Table 6. The free hydrazone ligand shows a strong band in the 2996-3625 cm^{-1} region. This band may be assigned due to ionic contribution from ν(OH) and ν(NH) stretching. This strong band is replaced by broadband in the complexes suggesting that the phenol character of the ligand is lost. The band corresponding to ν(C=O) is absent in the IR spectrum of the hydrazone ligand (Fig. 18-24). This observation supports the fact that the coordination of the hydrazone ligand to the vanadium centre in the enol form [59]. In the free ligand band due to ν(>C=N) stretching vibration remains at 1691 cm^{-1}, which shifts towards lower wave number on complexation, suggesting that the >C=N moiety is involved in bonding to the metal centre [60, 61]. The strong ν(V=O) stretch at ~942 cm^{-1} in all complexes is a clear indication of the dioxide nature of the complexes. A band appearing at 998 cm^{-1} in the hydrazone ligand due to the ν(N-H) stretch undergoes a shift to higher frequencies by 1018-1031 cm^{-1} on complexation [59-61]. A high-frequency shift of the ν(N-H) band is expected of the reduced repulsion between the lone pairs of adjacent nitrogen atoms [62].

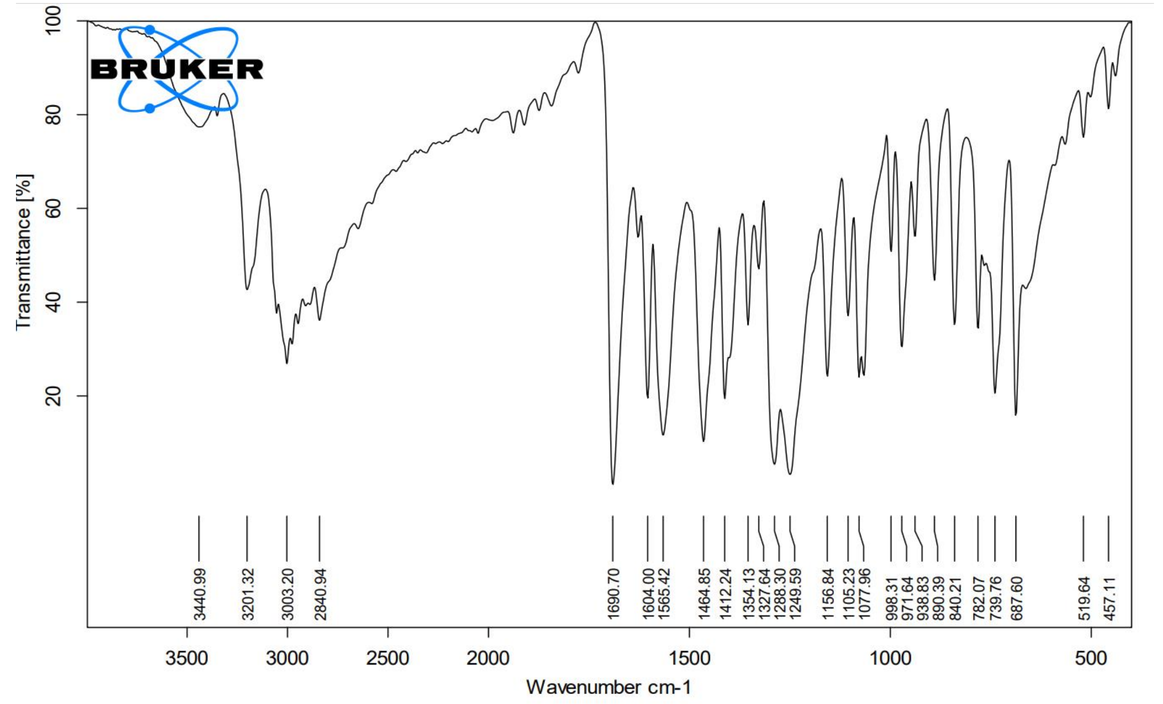

Fig. 18. FTIR spectrum of Ligand **H$_2$L**.

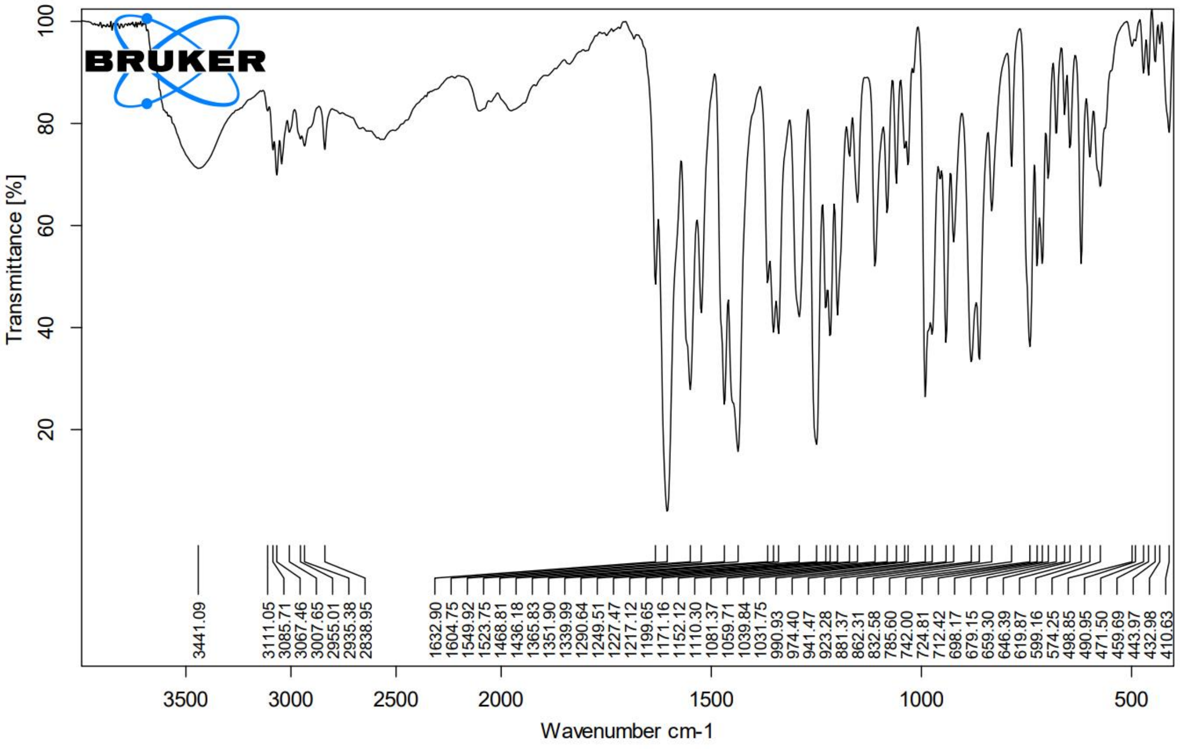

Fig. 19. FTIR spectrum of complex **1**.

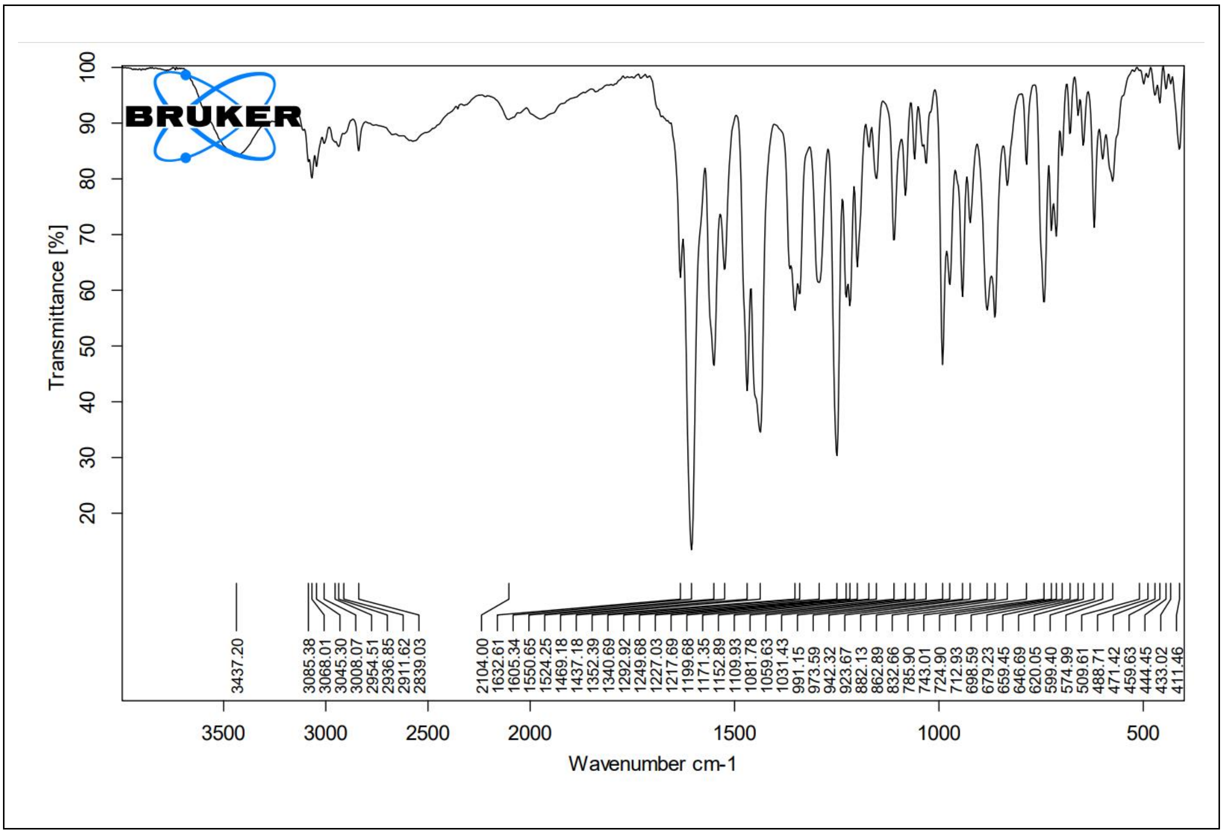

Fig. 20. FTIR spectrum of complex **2**.

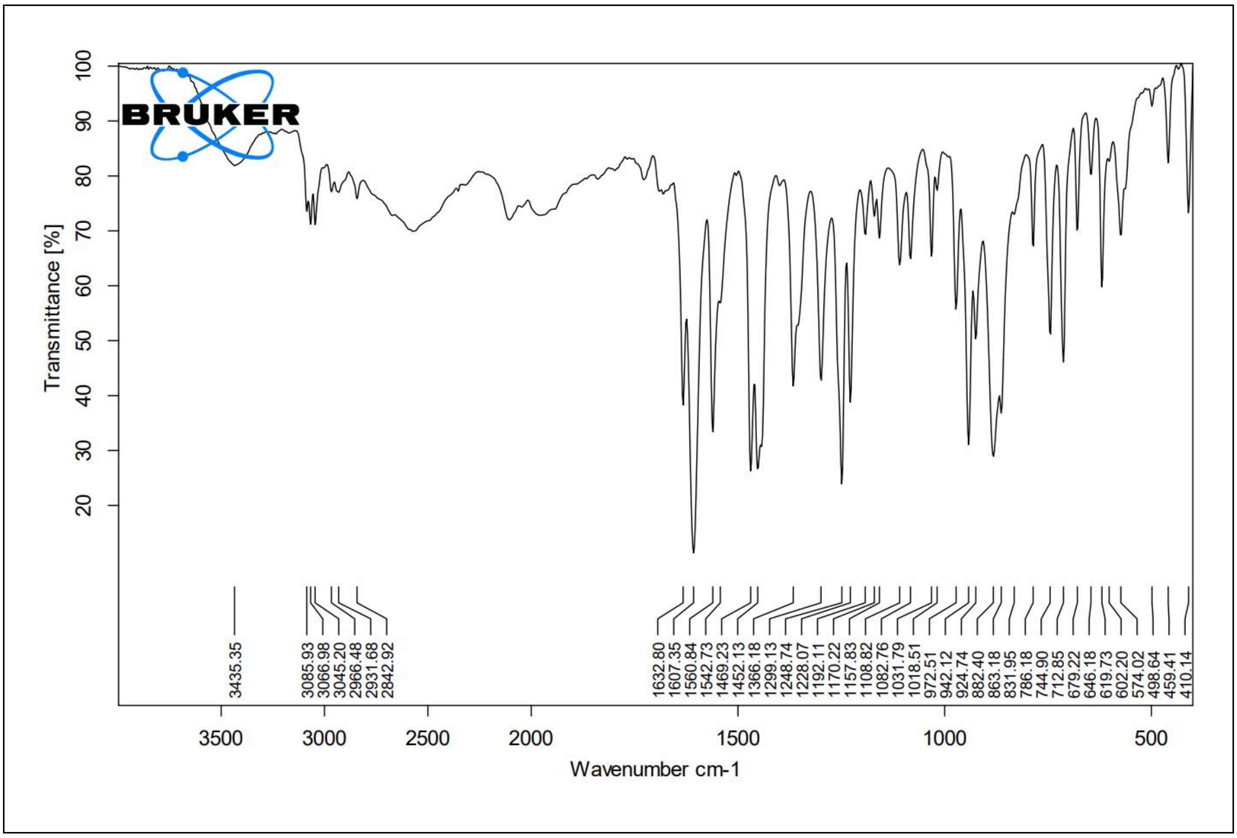

Fig. 21. FTIR spectrum of complex **3**.

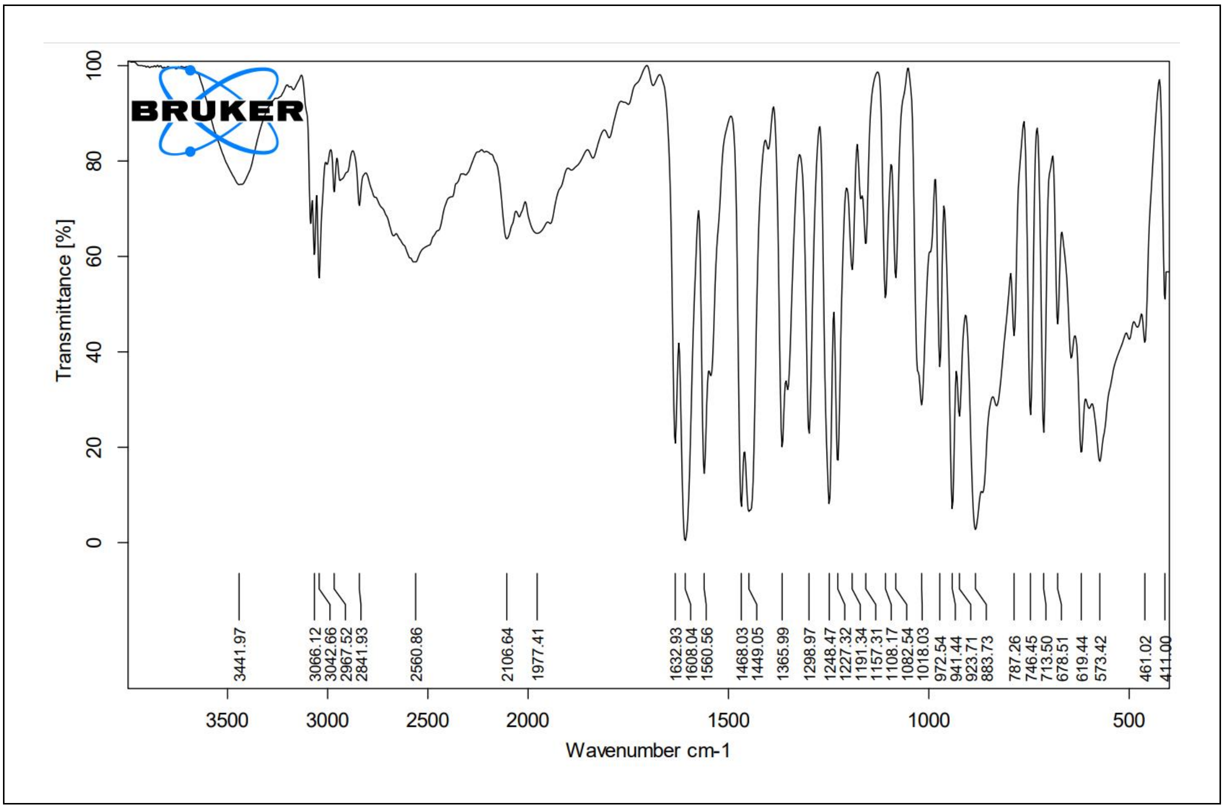

Fig. 22. FTIR spectrum of complex **4**.

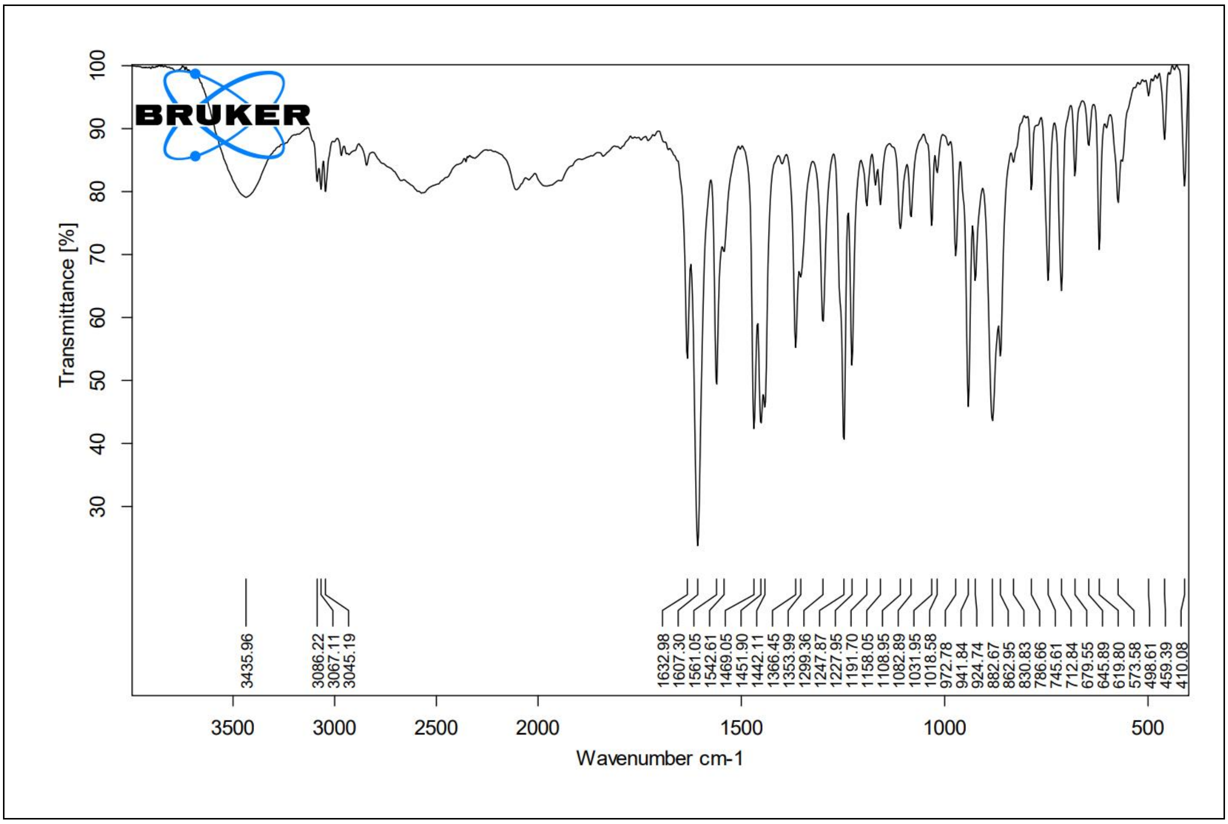

Fig. 23. FTIR spectrum of complex **5.**

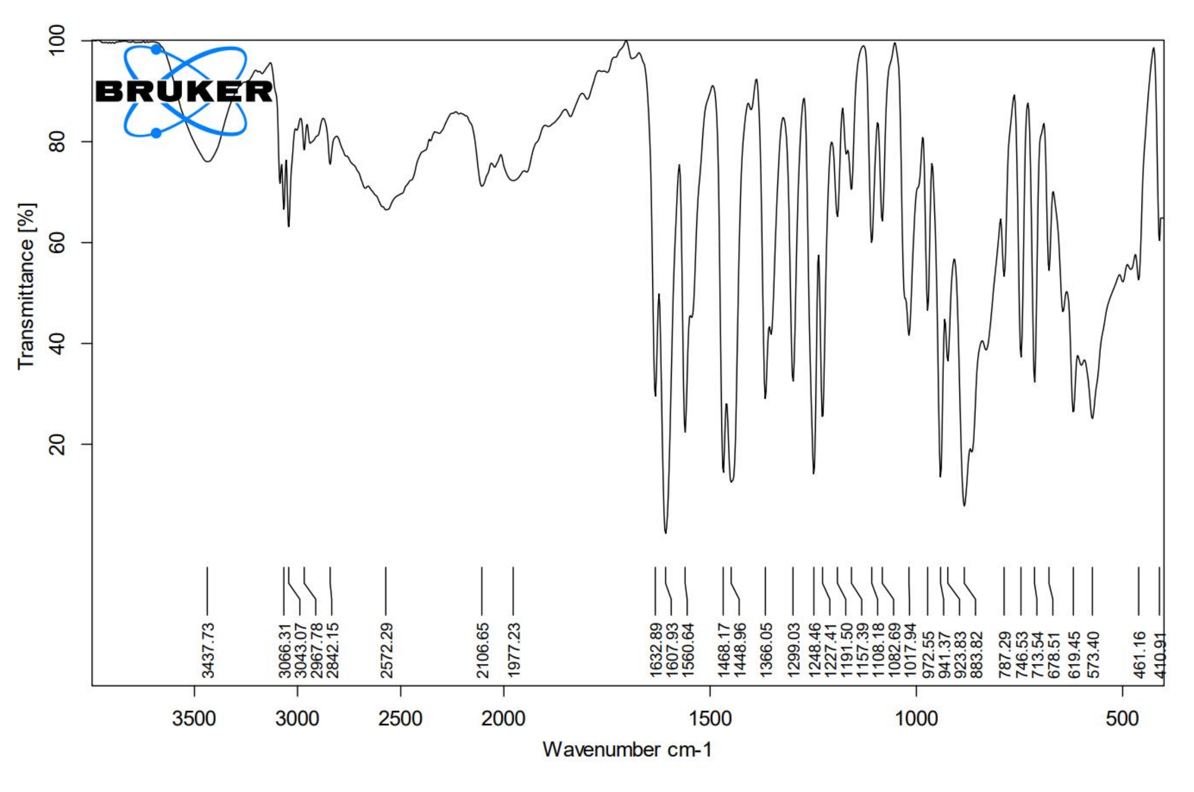

Fig. 24. FTIR spectrum of complex **6**.

Table 6 Some selected stretching frequencies (cm^{-1}) of ligand and complexes.

Compound	ν(>C=N)	ν(C-O)	ν(V=O)	ν(N-H)	ν(M-O)	ν(M-N)
H_2L	1691	-	-	998	-	-
1	1633	1291	942	1031	432	410
2	1633	1293	942	1031	433	411
3	1633	1299	942	1018	459	410
4	1633	1299	941	1018	461	411
5	1633	1299	942	1018	459	410
6	1633	1299	941	1018	461	410

3.7 Electronic spectral studies

Electronic spectra were recorded using DMSO solutions (1.0 × 10^{-3} M). All complexes display similar spectral profiles. Electronic spectra of complexes are shown in Fig 25. The electronic spectral data of complexes are presented in Table 7. The absorption bands in the region 286-293 nm are ascribed to an intra ligand charge transfer band, while the new bands of medium intensity appear at 415-431 nm are assigned to the ligand to metal charge transfer (LMCT) band which arises from the *p*-orbital lone pair of the phenolate oxygen atom to an empty d-orbital of vanadium (V) centre [63-68]. These complexes having V(V) (d^{10} system) did not show the d-d transition.

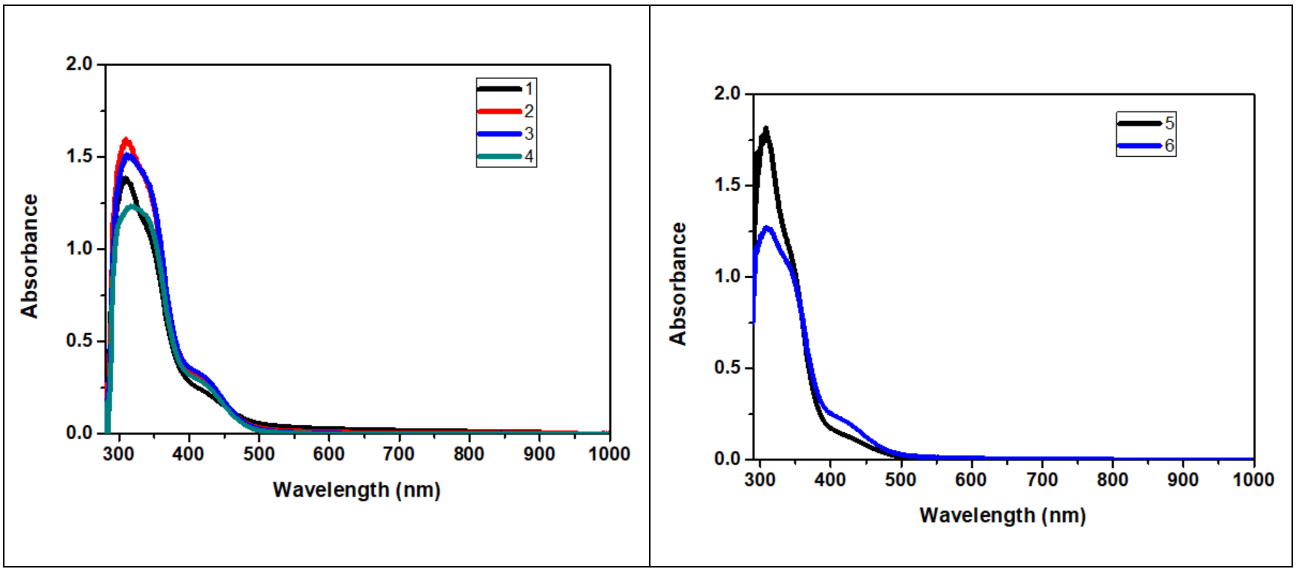

Fig. 25. Electronic spectra of complexes **1-6** in DMSO solution.

Table 7 Electronic spectral data of complexes **1-6**.

Compound	Intra ligand charge transfer (λ/nm)	LMCT (λ/nm)
1	288	416
2	286	415
3	288	415
4	293	418
5	286	431
6	286	427

3.8 Electrochemical studies

The electrochemical behaviours of complexes **1-6** was explored using cyclic voltammetry (CV) and differential pulse voltammetry (DPV). The cyclic voltammetry complexes **1-6** have been recorded in DMSO (1.0×10^{-3} M) using 0.1 M tetra butyl ammonium perchlorate (TBAP) with Ag/AgCl as reference electrode at a scan rate of 300 mV/s at 25°C. The cyclic voltammograms are shown in Fig. 26 and parameters are collected in Table 8.

Table 8 Electrochemical data of complexes **1-6**.

Complex	E_{pc} (V)	E_{pa} (V)	DE_c (V)	$E_{1/2}$ (V)	ΔE (V)
1	-0.771	-0.306	-0.648	-0.538	0.465
2	-0.827	--0.511	-0.660	-0.669	0.316
3	-0.816	-0.227	-0.672	-0.525	0.589
4	-0.818	-0.331	-0.654	-0.574	0.487
5	-0.821	-	-0.604	-	-
6	-0.865	-	-0.672	-	-

Complexes **1-6** show one reductive wave and one oxidative wave. Although oxidative wave for complexes **5** and **6** are not defined. The ΔE value of **1,** **3** and **4** is 465-589 mV, indicating the irreversible nature of redox waves. The cathodic peak potential in all complexes is within the range of the values reported in the literature for the electrode reaction $V(V) \xrightarrow{+1e^-} V(IV)$of the hydrazone vanadium complexes [69, 70]. The redox couple for complex **2** is found to be quasi reversible with ΔE = 316 mV [71, 72]. Same observations were obtained using DPV experiments. Again, one reduction peak potential was observed in all complexes (Fig. 27). Thus, experiments show that the reduction waves are due to one-electron transfer processes in complexes and these reduction processes are metal-centered reductions to the V(V) for all complexes **1-6** [73].

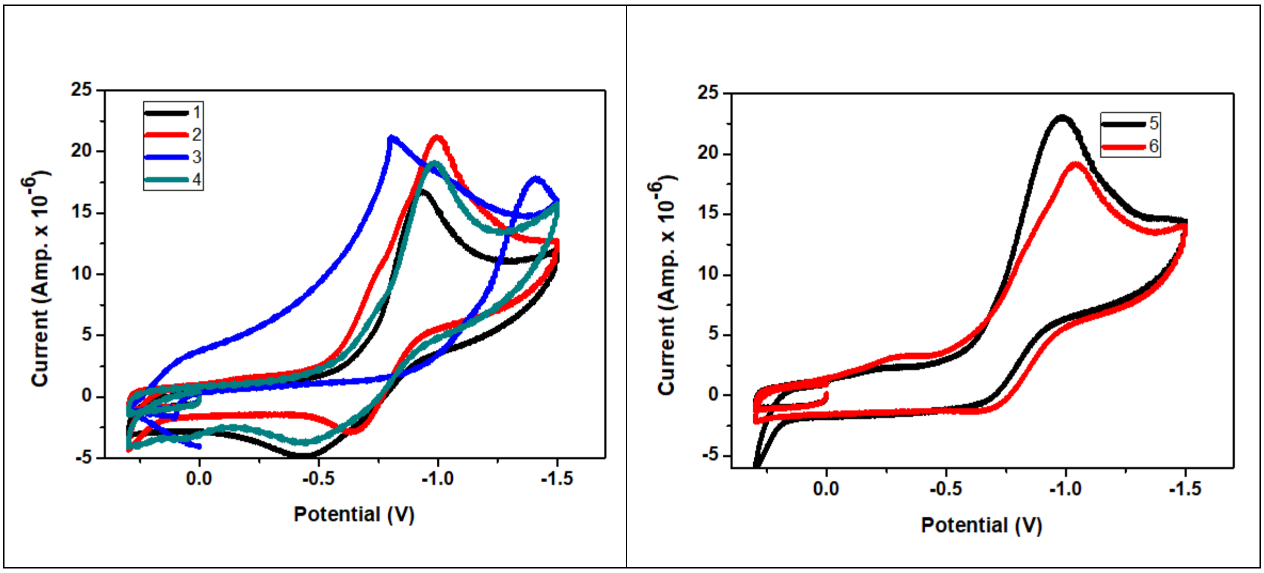

Fig. 26. Cyclic voltammograms of complexes **1-6** in DMSO (1.0 × 10^{-3} M) at an Ag/AgCl electrode at a scan rate of 300 mVs^{-1} and temperature of 20 ˚C.

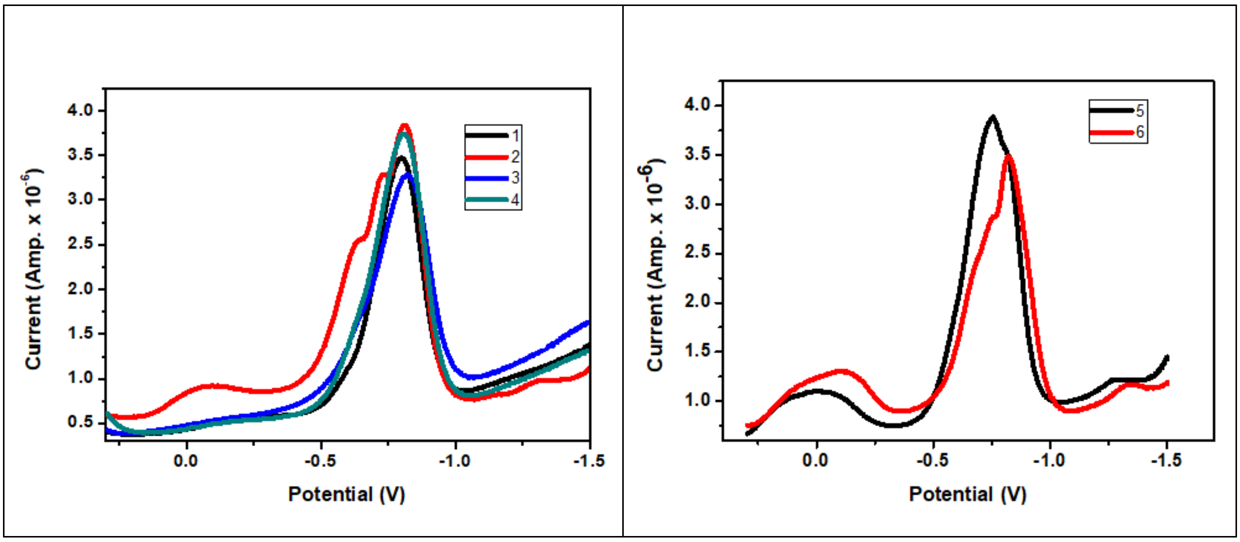

Fig. 27. Differential pulse voltammograms of complexes **1-6** at 20 ˚C in DMSO (1.0 × 10^{-3} M) solution (pulse amplitude = 50 mV).

3.9 Hirshfeld Surface Analyses

The Molecular Hirshfeld surfaces in the crystal structure of ligand were explored based on electron distribution. A molecular Hirshfeld surface [74] in the crystal structure was constructed based on the electron distribution calculated as the sum of spherical atom electron densities [75, 76]. For a given crystal structure and a set of spherical atomic densities, the Hirshfeld surface is unique [77]. The normalized contact distance (d_{norm}) based on both d_e and d_i (where d_e is the distance from a point on the surface to the nearest nucleus outside the surface and d_i is the distance from a point on the surface to the nearest nucleus inside the surface) and the vdW radii of the atom, as given by equation 2 enables identification of the regions of particular importance to intermolecular interactions [74]. The combination of d_e and d_i in the form of two-dimensional (2D) fingerprint plot [78, 79] provides a summary of intermolecular contacts in the crystal [74]. The Hirshfeld surfaces mapped with d_{norm} and 2D fingerprint plots were generated using the Crystal-Explorer 2.1 [80]. Graphical plots of the molecular Hirshfeld surfaces were mapped with d_{norm} used a red-white-blue colour scheme, where red highlights shorter contacts, white represents the contact around vdW separation and blue is for longer contact. Additionally, two further coloured plots representing shape index and curvedness based on local curvatures are also presented in this paper [81].

$$d_{\text{norm}} = \frac{d_{\text{i}} - r_{\text{i}}^{\text{vdW}}}{r_{\text{i}}^{\text{vdW}}} + \frac{d_{\text{e}} - r_{\text{e}}^{\text{vdW}}}{r_{\text{e}}^{\text{vdW}}} \qquad \ldots(2)$$

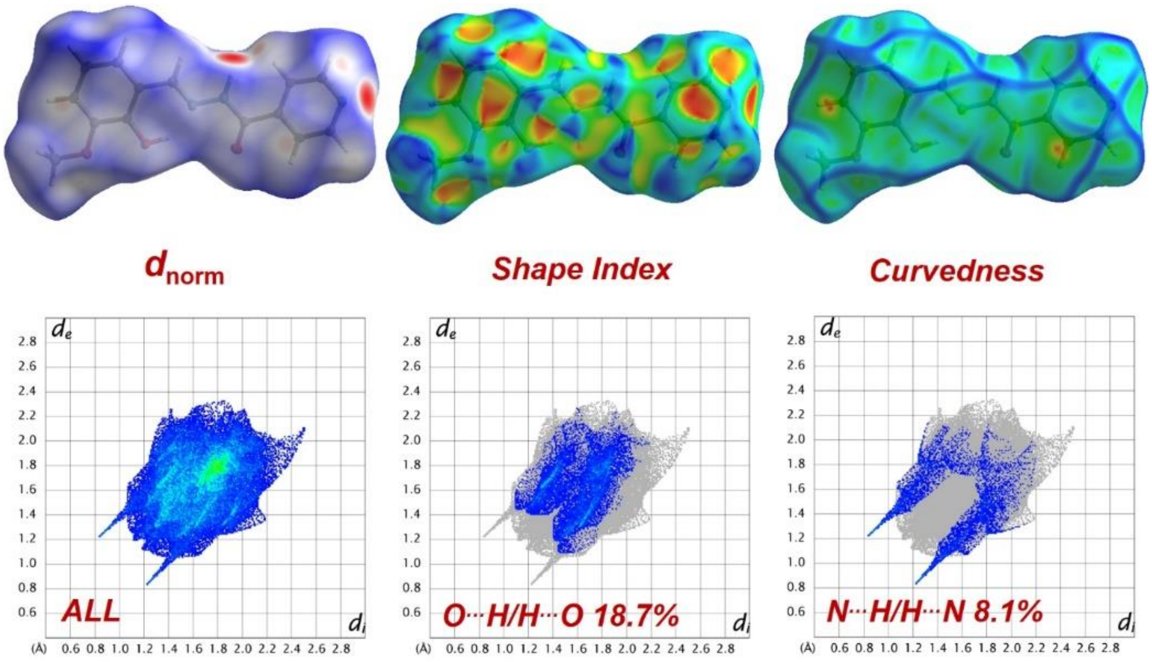

Fig. 28 (a) Hirshfeld surfaces mapped with d_{norm}, shape index and curvedness for the ligand; (b) Fingerprint plots for the ligand showing percentages of contact contributed to the total Hirshfeld surface area of the ligand molecule.

The Hirshfeld surfaces for ligand crystal structures mapped with d_{norm} surfaces. The Hirshfeld surface for the ligand is presented in Fig. 28 (a). For this ligand the d_{norm} surface is mapped between the range of -0.32 to 1.21 Å, shape index is constructed between -0.8 to 0.8 Å and the curvedness is mapped in the range -4.0 to 0.4 Å. All of these surfaces are presented transparently to offer better visualization of all the aromatic rings present in the ligand. The O···H and N···H interactions which are discussed in the molecular structure description (*vide supra*) can be visualized as different types of spots in the d_{norm} surface. The large circular deep red depressions in d_{norm} surfaces indicative of O···H and N···H hydrogen bonding interactions as a faint red shaded area.

Another important result of the Hirshfeld surface analyses is the fingerprint plots (Fig. 28 (b)). In fingerprint plots, the opposite regions are presented in the mode where one molecule act as a donor ($d_{\text{e}} > d_{\text{i}}$) and another behaves as an acceptor ($d_{\text{e}} < d_{\text{i}}$). Besides, the total fingerprint plots have been split to focus on the particular atom pair close contacts. This enabled the separation of contributions from different interaction types, which usually overlap in the full fingerprint. The fingerprint plot of the ligand possess equal-sized spikes which represent interactions of the ligand (vide infra). The most important interaction in the ligand is the O···H/H···O interaction which appears as discrete spikes 1.1 Å < (d_e + d_i) < 2.1 Å in the total fingerprint plot of the ligand. The Hirshfeld surface calculation revealed that this interaction is contributing 18.7% of the total Hirshfeld surface area. Another important interaction in the ligand is the N···H/H···N interaction which appears as discrete spikes 0.8 Å < (d_e + d_i) < 2.2 Å in the total fingerprint plot of the ligand and contributes 8.1% of the total Hirshfeld surface area.

3.10 Molecular modelling

Optimization of the geometry of molecules is the primary step to determine the structural parameters such as bond distances and bond angles. The optimized structures are obtained using DFT studies at B3LYP/ LANL2DZ basic set level. The optimized structures are shown in Fig. 29 and bond distances and angles are collected in Table 9. The geometry of the vanadium(V) centre is distorted square pyramidal and distorted trigonal pyramidal [82]. The Schiff base ligand is diatonic (L^2) with ONO donor sites. The VO_2^+ entity accommodated in the ONO binding site of tridentate ligand yields $[V(O_2)L]^-$ anion. One imidazolium ion satisfies the charge of the unit. The double bonds between V(V) dioxide oxygen atoms of 1.630-1.636 Å in distorted square pyramidal geometry are comparable to those reported in similar complexes [83]. The fourth equatorial position is occupied by the second dioxo oxygen atom.

The distortion in the geometry is given by the structural parameter τ, where $\tau = 0$ for square pyramidal and $\tau = 1$ for trigonal bipyramidal geometry [84, 85]. The $\tau_5 = 0.759\text{-}0.770$ value for **1**, **2** and **3** are very close to **1** authenticating the distorted trigonal bipyramidal geometry around the V(V) centre. For complexes **4**, **5** and **6** the value of $\tau = 0.198$, 0.010 and 0.385 suggesting the distorted square planar geometry of V(V) centers.

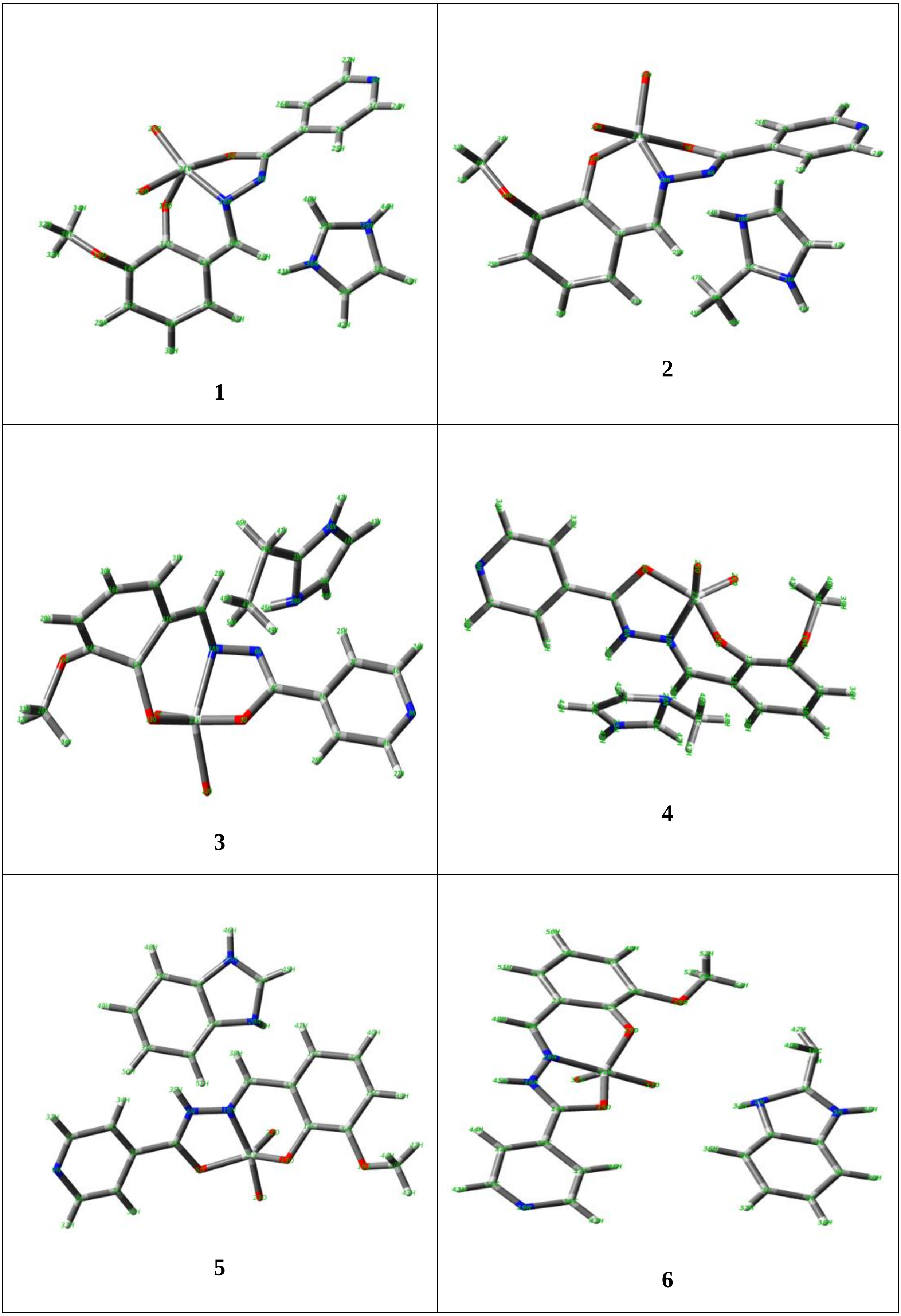

1

2

3

4

5

6

Fig. 29. Optimized structure of complexes **1-6.**

Table 9 Optimized bond lengths(Å) and angles (°) of complexes **1-6**.

1			
Bond lengths			
V(21)-O(5)	1.882	V(21)-O(23)	1.860
V(21)-O(13)	1.793	V(21)-N(18)	1.895
V(21)-O(22)	1.860		
Bond angles			
O(5)-V(21)-O(13)	112.236	O(13)-V(21)-O(22)	89.998
O(5)-V(21)-N(18)	67.815	O(13)-V(21)-O(23)	90.009
O(5)-V(21)-O(22)	89.995	N(18)-V(21)-O(22)	157.798
O(5)-V(21)-O(23)	90.002	N(18)-V(21)-O(23)	22.199
O(13)-V(21)-N(18)	97.546	O(22)-V(21)-O(23)	70.161
2			
Bond lengths			
V(21)-O(5)	1.864	V(21)-O(23)	1.860
V(21)-O(13)	1.765	V(21)-N(18)	1.896
V(21)-O(22)	1.860		
Bond angles			
O(5)-V(21)-O(13)	111.846	O(13)-V(21)-O(22)	90.002
O(5)-V(21)-N(18)	68.187	O(13)-V(21)-O(23)	90.000
O(5)-V(21)-O(22)	89.999	N(18)-V(21)-O(22)	158.174
O(5)-V(21)-O(23)	89.998	N(18)-V(21)-O(23)	21.824
O(13)-V(21)-N(18)	98.613	O(22)-V(21)-O(23)	70.558
3			
Bond lengths			
V(21)-O(5)	1.854	V(21)-O(23)	1.859
V(21)-O(13)	1.780	V(21)-N(18)	1.895
V(21)-O(22)	1.860		
Bond angles			
O(5)-V(21)-O(13)	112.160	O(13)-V(21)-O(22)	90.003
O(5)-V(21)-N(18)	68.376	O(13)-V(21)-O(23)	90.002
O(5)-V(21)-O(22)	89.998	N(18)-V(21)-O(22)	158.371
O(5)-V(21)-O(23)	90.009	N(18)-V(21)-O(23)	21.627
O(13)-V(21)-N(18)	98.338	O(22)-V(21)-O(23)	70.745
4			
Bond lengths			
V(21)-O(5)	1.871	V(21)-O(23)	1.636
V(21)-O(13)	1.869	V(21)-N(18)	1.900
V(21)-O(22)	1.636		
Bond angles			
O(5)-V(21)-O(13)	139.829	O(13)-V(21)-O(22)	87.415

O(5)-V(21)-N(18)	78.869	O(13)-V(21)-O(23)	100.342
O(5)-V(21)-O(22)	84.672	N(18)-V(21)-O(22)	162.968
O(5)-V(21)-O(23)	119.775	N(18)-V(21)-O(23)	93.159
O(13)-V(21)-N(18)	102.343	O(22)-V(21)-O(23)	98.834
5			
Bond lengths			
V(21)-O(5)	1.883	V(21)-O(23)	1.636
V(21)-O(13)	1.856	V(21)-N(18)	1.894
V(21)-O(22)	1.636		
Bond angles			
O(5)-V(21)-O(13)	133.886	O(13)-V(21)-O(22)	104.135
O(5)-V(21)-N(18)	82.626	O(13)-V(21)-O(23)	92.661
O(5)-V(21)-O(22)	121.978	N(18)-V(21)-O(22)	94.852
O(5)-V(21)-O(23)	84.845	N(18)-V(21)-O(23)	21.034
O(13)-V(21)-N(18)	94.515	O(22)-V(21)-O(23)	93.534
6			
Bond lengths			
V(31)-O(15)	1.850	V(31)-O(33)	1.634
V(31)-O(23)	1.826	V(31)-N(28)	1.896
V(31)-O(32)	1.630		
Bond angles			
O(15)-V(31)-O(23)	121.813	O(23)-V(31)-O(32)	122.433
O(15)-V(31)-N(28)	86.029	O(23)-V(31)-O(33)	90.008
O(15)-V(31)-O(32)	115.666	N(28)-V(31)-O(32)	90.994
O(15)-V(31)-O(33)	93.965	N(28)-V(31)-O(33)	22.436
O(23)-V(31)-N(28)	89.977	O(32)-V(31)-O(33)	89.024

3.11 Frontier Molecular Orbital (FMO) analysis

The ground state electronic structures of the complexes were determined based on the optimized ground state geometry method of the synthesized complexes. The data of frontier molecules orbital (FMO) analysis were analyzed to understand the various structural features of the complexes in different viewpoints such as UV-Vis and FTIR spectra, optical properties, charge transfer, reactivity and interactions in the chemical molecule [86]. The energy gap (ΔE_g) between the highest occupied and lowest unoccupied molecular orbitals provides information about the reactivity and nature of complexes. The energy profile of the investigated complexes is shown in Fig. 30 and computed structural parameters and their values are given in Table 10. The ΔE_g of the present complexes have the trend: **6** (-2.252 eV) < **1** (-2.506 eV) < **3** (-2.544 eV) < **2** (-2.560 eV) < **5** (-2.664) < **4** (-2.777 eV).

The ΔE_g, E_{HOMO}, E_{LUMO} are used to predict the global reactivity parameters. These reactivity parameters also describe the stability and reactivity of the complex molecules. Values of different global reactivity parameters such as electronegativity (χ), ionization potential (IP), electron affinity (EA), chemical potential(μ), global hardness (Ƞ), softness (S) and electrophilicity index(ω) are evaluated using correlation-based on Koopmans theorems (Table 10) [87]. In complexes, **1**, **2** and **3** HOMO is occupied on the skeleton of a tridentate ligand having geometry distorted trigonal pyramidal, whereas in remaining complexes (**4**, **5** and **6**) HOMO is on VO_2^+ moiety. Similarly, LUMO is occupied on imidazolium ions except in **5** where it is localized on the skeleton of the tridentate ligand. The ΔE_g inversely associated with the reactivity and hardness of complexes. Also, small ΔE_g reveals easy charge transfer, which may additionally increase the biological activity of complexes.

The spin density plots of **1-6** are shown in Fig. 31 the spin density distribution in the anions and cations are unexpected. In complexes **1**, **2** and **6** the spin density distribution mostly incorporates the anionic part of the complexes. In complexes **3** and **4** it incorporates both anion and cation of the complexes. But in **5** it is only localized on the cationic part of the complex.

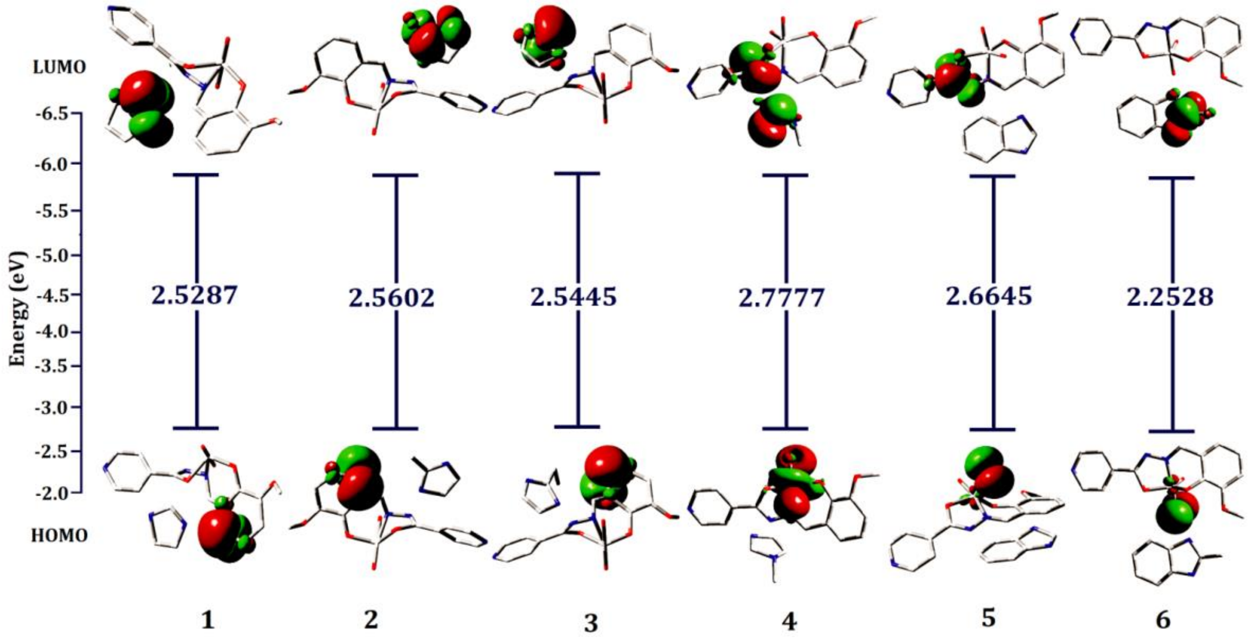

Fig. 30. Energy profile diagram of complexes **1-6**.

Table 10 Global reactivity descriptors vanadium complexes in eV calculated by DFT/B3LYP/LANL2DZ basic.

Molecular properties	**Mathematical description**	**1**	**2**	**3**	**4**	**5**	**6**
E_{HOMO}	Energy of HOMO	-6.397	-6.127	-6.544	-6.275	-6.001	-6.104
E_{LUMO}	Energy of LUMO	-3.869	-3.567	-3.856	-3.497	-3.337	-3.851
Energy gap	$\Delta E_g = E_{HOMO} - E_{LUMO}$	2.528	2.560	2.544	2.777	2.664	2.252
Ionization potential (IP)	$IP = -E_{HOMO}$	6.397	6.127	6.544	6.275	6.001	6.104
Electron Affinity (EA)	$EA = -E_{LUMO}$	3.869	3.567	3.856	3.497	3.337	3.851
Electronegativity (χ)	$(\chi) = -½\ (E_{Homo} + E_{Lumo})$	5.133	4.847	5.200	4.886	4.669	4.977
Chemical Potential(μ)	$\mu = ½\ (E_{Homo} + E_{Lumo})$	-5.133	-4.847	-5.200	-4.886	-4.669	-4.977
Global Hardness (η)	$(\eta) = -½\ (E_{Homo} - E_{Lumo})$	1.264	1.280	1.272	1.388	1.332	1.126
Softness (S)	$(S) = 1/2\eta$	0.395	0.390	0.393	0.360	0.375	0.444
Electrophilicity index(ω)	$\omega = \mu^2/2\eta$	9.235	9.176	10.628	8.599	8.182	10.999

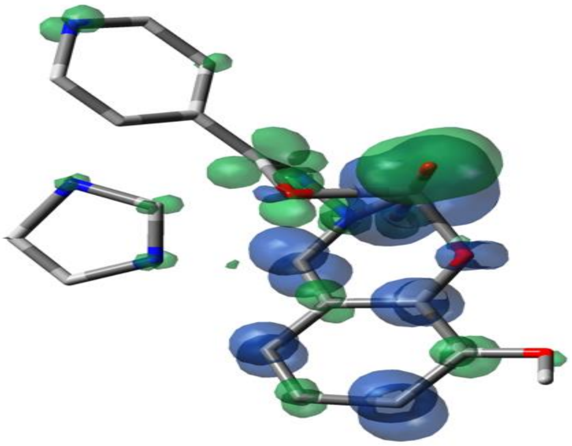

1

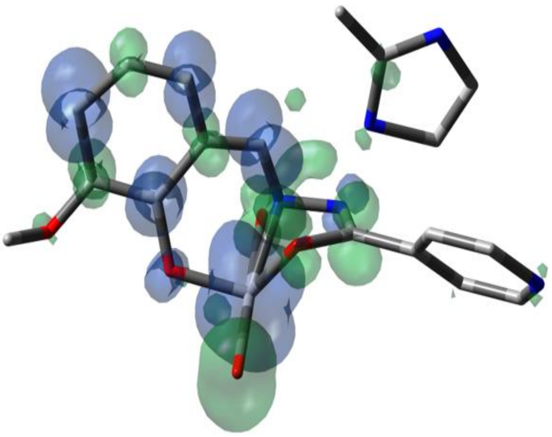

2

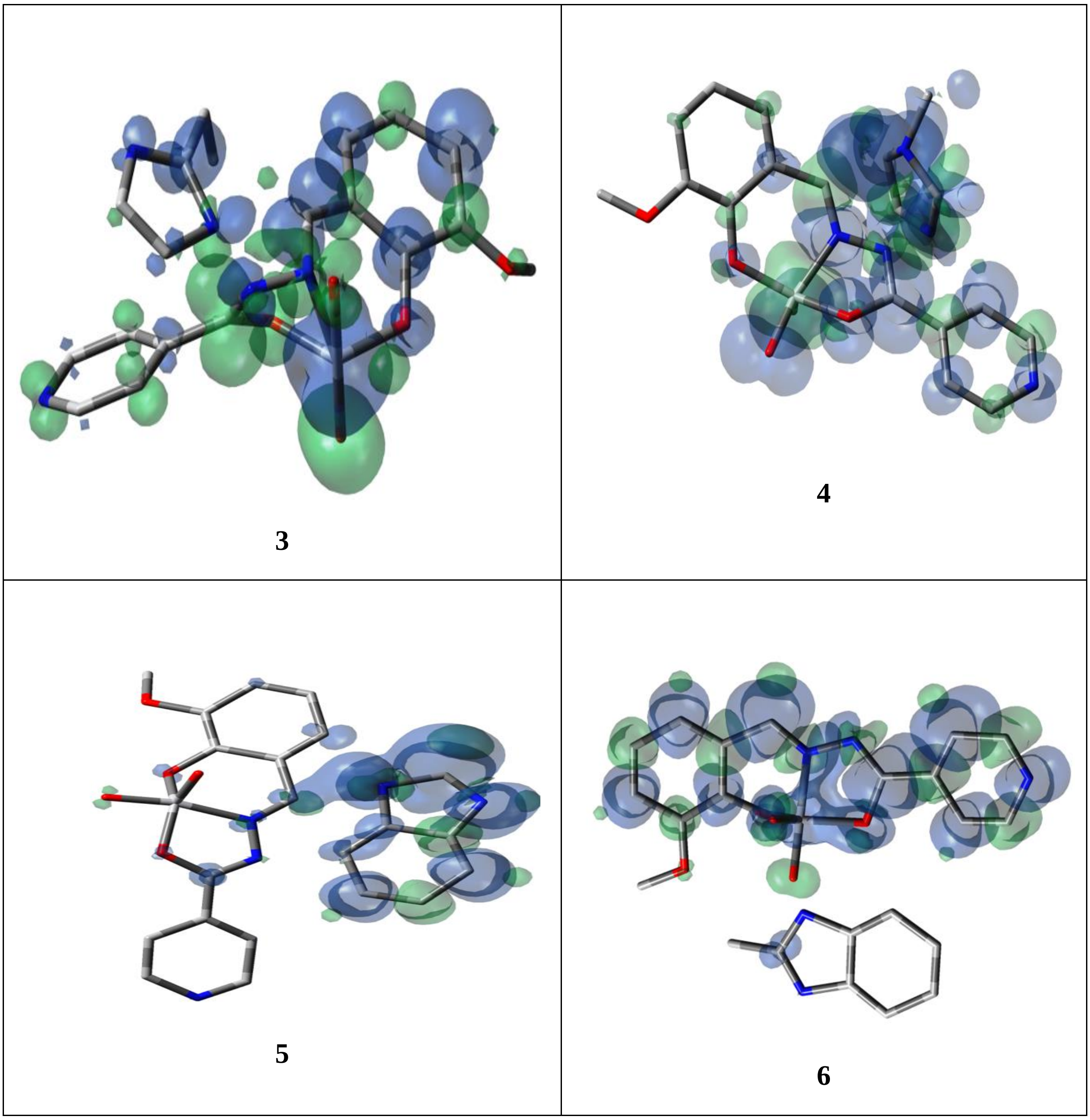

3

4

5

6

Fig. 31. Spin density plot of complexes **1-6**.

3.12 Thermogravimetric analysis

Thermal analysis of the complexes was carried in an atmosphere of nitrogen at a heating rate of 10 °C /min. The thermal analysis of complexes is recorded in the temperature range of 25-650 °C. All complexes **1-6** are stable up to 300 ^{o}C and thereafter they decompose exothermically and showed two-step decomposition patterns. The thermograph of complexes **1-6** are shown in Fig. 32. In all complexes, the first decomposition pattern is observed at around ~350 ^{o}C which is due to the loss of uncoordinated counter ions that is the imidazolium ion. Upon further increment of the temperature, second step decomposition is observed around ~400 °C is due to loss of ligand moiety. In Complex **4** decomposition is observed at around 100 °C is due to the presence of some moisture in the compound. The final step in all complexes is observed at ~560 °C further upon no decomposition is observed. The final product was obtained as a metal oxide that is V_2O_5 [88, 89].

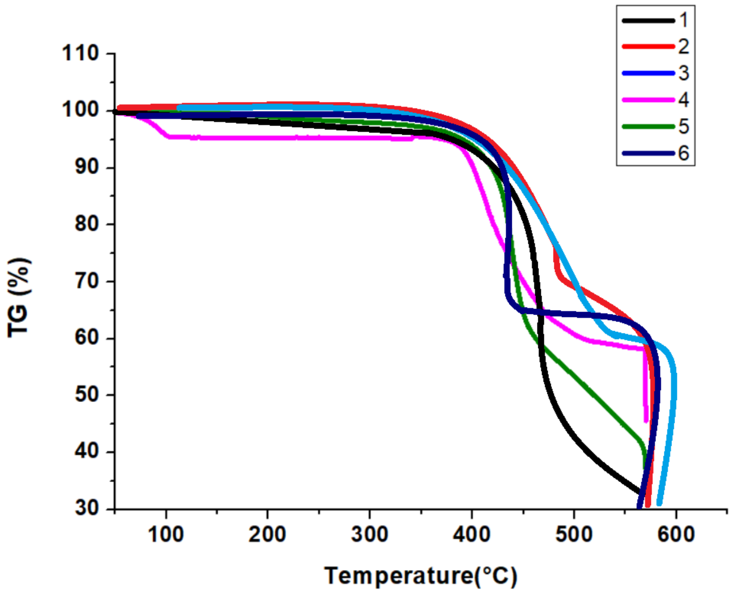

Fig. 32. TGA graph of complexes **1-6**.

3.13 Antidiabetic activity

3.13.1 α-Glucosidase inhibition activity

The α-glucosidase inhibitory activity was assayed by using pNPG as a substrate. Fig. 33 shows the results of % inhibition *vs.* concentration. The IC_{50} values of complexes **1-6** are collected in Table 11. The major micro constituents in the biological system are carbohydrates, proteins and fats. The dominant constituents of carbohydrates are glucose, fructose, maltose and sucrose. These constituents can be easily absorbed into the blood-stream from the gastrointestinal tract. The role of α-glucosidase and α-amylase are to transform most of the polysaccharides and insoluble polysaccharides into absorbable Monosaccharides. Hence, diabetes and obesity could be controlled by inhibiting the enzyme activity of α-glucosidase and α-amylase to wait for the absorption of these carbohydrates from our diets. The α-glucosidase inhibition study of complexes **1-6** is in agreement with what was reported in the literature [23, 27, 90-92]. On the basis of concentration-dependent activity is the order **6** > **5** > **4** > **3** > **2** > **1**. Among these complexes, complex **6** revealed good inhibition by being the most active complex in the series. The observed result is consistent with our previous findings on similar vanadium complexes [23, 27]. Based on the above-obtained results, these complexes may be potent inhibitors.

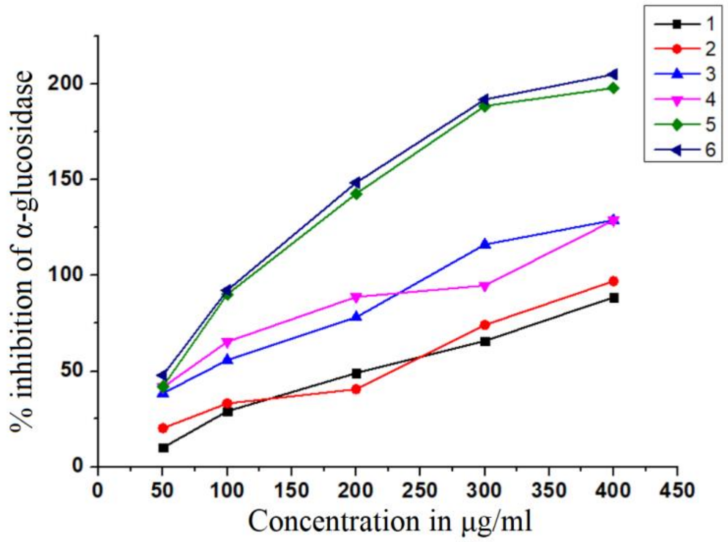

Fig. 33. α-Glucosidase inhibition graph of complexes **1-6**.

Table 11 α-Glucosidase inhibitory activity data of complexes **1-6**.

Complex	IC_{50} (μg/mL)	Antidiabetic activity (μg^{-1})
1	199.11	5.02
2	225.09	4.44
3	87.53	11.42
4	69.95	14.29
5	60.17	16.61
6	53.88	18.55

3.13.2 β-Glucosidase inhibition activity

The β-glucosidase inhibition data with the substrate pNPG was also collected. The IC_{50} values are shown in Table 12 and graphical presentation data are shown in Fig. 34. The IC_{50} values for β-glucosidase inhibition activity were ranged from 200-1000 μg/ml. The inhibition data are similar to the previously reported results [23, 93]. The inhibitory data showed that complex **4** exhibited the strongest inhibition and **6** showed the lowest inhibition.

It is found that these complexes showed higher inhibitory activity on β-glucosidase than acarbose, which was taken as a positive control during inhibition measurements. Therefore, we conclude that the present complexes are potent inhibitors and may be considered antidiabetic drugs.

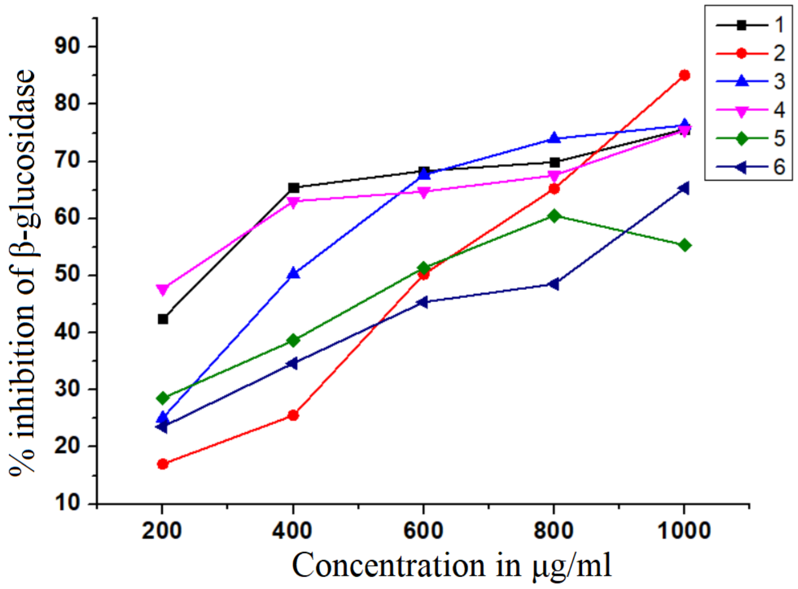

Fig. 34. β-Glucosidase inhibition graph of complexes **1-6**.

Table 12 β-Glucosidase inhibitory activity data of complexes **1-6**.

Complex	IC_{50} (µg/mL)	Antidiabetic activity (μg^{-1})
1	266.52	3.75
2	609.61	1.64
3	400.45	2.49
4	227.45	4.39
5	586.20	1.70
6	843.41	1.18

3.13.3 α-Amylase inhibition activity

The α-amylase activity of complexes **1-6** were also measured. The IC_{50} and amylase activity are collected in Table 13. A plot of % inhibition *vs.* concentration is shown in Fig. 35. α-amylase is involved in the inhibition of carbohydrate metabolism for the treatment of type II diabetes. Acarbose was taken as control. Acarbose is a tetrasaccharide and it inhibits *in vitro* and *in vivo* such as dextrinase, maltose, glucoamylase, sucrose and pancreatic amylase. Therefore, it is used as an inhibitor in inhibition steady of α-amylase and α-glucosidase inhibition [94, 95]. Complexes **1-6** showed reasonable fair activity as compared to the control. Among these complexes, **1** and **2** exhibited moderate and weak activity respectively, compared to the remaining complexes. Complexes having electron repelling moiety showed better activity. All these complexes showed concentration-dependent activity and the inhibitory activity were observed to increase as a function of the concentration of complexes.

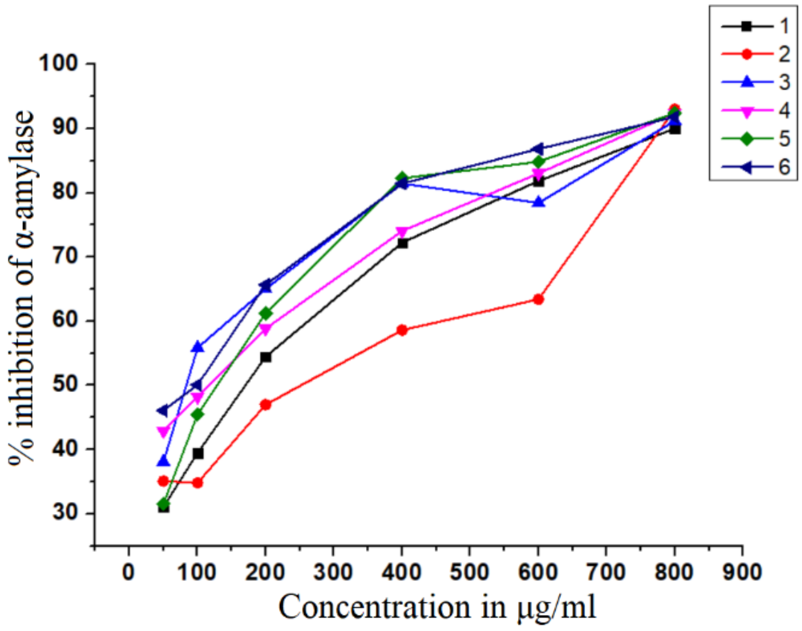

Fig. 35. α-Amylase inhibition graph of complexes **1-6**.

Table 13 α-Amylase inhibitory activity data of complexes **1-6**.

Complex	IC$_{50}$ (µg/mL)	Antidiabetic activity (µg^{-1})
1	173.30	5.77
2	265.21	3.77
3	82.99	12.04
4	116.93	8.55
5	131.82	7.58
6	100.65	9.99

4 Conclusions

In this work dioxidovanadium(V) complexes were synthesized using tridentate hydrazone Schiff base. The Schiff base and dioxidovanadium(V) complexes were characterized by using FTIR, NMR, single-crystal X-ray diffraction analysis, powder X-ray diffraction analysis, mass spectrometry, Hirshfeld analysis and DFT calculations. Six new dioxidovanadium(V) complexes (**1-6**) of ONO-Schiff base hydrazone has been synthesized using (H_2L**)**, H_2L = isonicotinic acid (2-hydroxy-3-methoxy-benzylidene)-hydrazide ligand. Due to small formed crystals, and the problem with complex recrystallization, complex decomposition, the single X-ray crystal structure could not be determined. These complexes have been characterized for their spectroscopic and redox properties. These complexes having V(V) (d^0 system) did not show a d-d transition in electronic spectra. The geometry of these complexes can be described in terms of trigonal bipyramidal or square pyramidal. Complexes **1-6** show one reductive wave and one oxidative wave. Although oxidative wave for complexes **5** and **6** are not defined. The ΔE value of **1, 3 & 4** is 465-589 mV, indicating the irreversible nature of redox waves. Besides, *in vitro* α-glucosidase, β-glucosidase inhibition activity and α-amylase inhibition activity results proved that these complexes are promising anti-diabetic agents.

References

1 Vandium and its Role in Life; H. Sigel, A. Sigel, Eds.; Metal Ions in Biological Systems, Vol. 31; Marcel-Dekker: New York, 1995.

2 Y. Shechter, S.J.D. Karlish, Nature 284 (1980) 556–558.

3 D. Rehder, Bioinorganic Vanadium Chemistry, John Wiley & Sons, Chichester, U.K. 2008.

4 R.R. Eady, Coord. Chem. Rev. 237 (2003) 23–30.

5 K.H. Thompson and C. Orvig, Coord. Chem. Rev. 219–221 (2001) 1033–1053.

6 I. Osinska-Krolicka, H. Podsiadly, A. Bukietynska, J. Inorg. Biochem. 98 (2004) 2087–2098.

7 T. Hirao, Chem. Rev. 97 (1997) 2707–2724.

8 C. Bolm, Coord. Chem. Rev. 237 (2003) 245–256.

9 A.G.J. Ligtenbarg, R. Hage, B.L. Feringa, Coord. Chem. Rev. 237 (2003) 89–101.

10 S. Takizawa, T. Katayama, H. Sasai, Chem. Commun. (2008) 4113–4122.

11 F. Cavani, N. Ballarini, A. Cericola, Catal. Today 127 (2007)113–131.

12 S.K. Hanson, R. Wu, L.A.P. Silks, Org. Lett. 13 (2011) 1908–1911.

13 N. Mizuno, K. Kamata, Coord. Chem. Rev. 255 (2011) 2358–2370.

14 K.H. Thompson, C. Orvig, J. Inorg. Biochem. 100 (2006) 1925–1935.

15 H. Sakurai, Y. Yoshikawab, H. Yasui, Chem. Soc. Rev. 37 (2008) 2383-2392.

16 D.A. Barrio, S.B. Etcheverry, Curr. Med. Chem. 17 (2010) 3632-3642.

17 G.R. Willskya, L.H. Chi, M. Godzala, P.J. Kostyniaka, J.J. Smee, A.M. Trujillo, J.A. Alfanoa, W. Ding, Z. Huc, D.C. Crans, Coord. Chem. Rev. 255 (2011) 2258–2269.

18 J.H. McNeill, V.G. Yuen, S. Dai, C. Orvig, Mol. Cell. Biochem. 153 (1995) 175-180.

19 W. Plass, A. Pohlmann, H.-P. Yozgatli, J. Inorg. Biochem. 80 (2000) 181-183.

20 W. Plass, Coord. Chem. Rev. 237 (2003) 205-212.

21 D. Rehder, Coord. Chem. Rev. 182 (1999) 297-322.

22 M.R. Maurya, Coord. Chem. Rev. 237 (2003) 163-181.

23 N. Patel, A.K. Prajapati, R.N. Jadeja, R.N. Patel, S.K. Patel, I.P. Tripathi, N. Dwivedi, V.K. Gupta, R.J. Butcher, Polyhedron 180 (2020) 114434.

24 N. Patel, A.K. Prajapati, R.N. Jadeja, I.P. Tripathi, N. Dwivedi, J. Coord. Chem. 73 (2020) 1131-1146.

25 R.N. Patel, Y.P. Singh, Y. Singh, R.J. Butcher, J.P. Jasinski, Polyhedron 133 (2017) 102-109.

26 R.N. Patel, Y.P. Singh, J. Mol. Struct. 1153 (2018) 162-169.

27 N. Patel, A.K. Prajapati, R.N. Jadeja, R.N. Patel, S.K. Patel, V.K. Gupta, I.P. Tripathi, N. Dwivedi, Inorg. Chim. Acta 493 (2019) 20-28.

28 F. Zhuge, Inorg. Chem. 48 (2009) 10249-10256.

29 M. Meot-Ner, Chem. Rev. 112 (2012) 22–103.

30 J.K. Maclaren, C. Janiak, Inorg. Chim. Acta 389 (2012) 183–190.

31 D. Mekhatria, S. Rigolet, C. Janiak, A. Simon-Masseron, M.A. Hasnaoui, A. Bengueddach, Cryst. Growth Des. 11 (2011) 396–404.

32 B.M. Drašković, G.A. Bogdanović, M.A. Neelakantan, A.-C. Chamayou, S. Thalamuthu, Y.S. Avadhut, J. Schmedt auf der Günne, S. Banerjee, C. Janiak, Cryst.

Growth Des. 10 (2010) 1665–1676.

33 B. Gil-Hernández, H.A. Hoppe, J.K. Vieth, J. Sanchiz, C. Janiak, Chem. Commun. 46 (2009) 8270–8272.

34 H.W. Roesky, M. Andruh, Coord. Chem. Rev. 236 (2003) 91–119.

35 L. Brammer, Chem. Soc. Rev. 33 (2004) 476–489.

36 I. Cvrtila, V. Stilinović, B. Kaitner, Cryst. Eng. Comm. 15 (2013) 6585–6593.

37 Bruker, SMART (Version 5.631), SAINT (Version 6.45) and SADABS (Version 2.05), Bruker AXS Inc., Madison, Wisconsin, USA (2003).

38 G.M. Sheldrick, SHELXS97, SHELXL97, University of Gottingen, Germany (1997).

39 A.L. Spek, PLATON for Windows. September (1999) Version, University of Utrecht, Netherlands (1999).

40 M. Nardelli, J. Appl. Crystallogr. 28 (1995) 659.

41 M.J. Frisch, G.W. Trucks, H.B. Schlegel, G.E. Scuseria, M.A. Robb, J.R. Cheeseman, G. Scalmani, V. Barone, B. Mennucci, G.A. Petersson, H. Nakatsuji, M. Caricato, X. Li, H.P. Hratchian, A.F. Izmaylov, J. Bloino, G. Zheng, J.L. Sonnenberg, M. Hada, M. Ehara, K. Toyota, R. Fukuda, J. Hasegawa, M. Ishida, T. Nakajima, Y. Honda, O. Kitao, H. Nakai, T. Vreven, J.A. Montgomery Jr., J.E. Peralta, F. Ogliaro, M. Bearpark, J.J. Heyd, E. Brothers, K.N. Kudin, V.N. Staroverov, T. Keith, R. Kobayashi, J. Normand, K. Raghavachari, A. Rendell, J.C. Burant, S.S. Iyengar, J. Tomasi, M. Cossi, N. Rega, J.M. Millam, M. Klene, J.E. Knox, J.B. Cross, V. Bakken, C. Adamo, J. Jaramillo, R. Gomperts, R.E. Stratmann, O. Yazyev, A.J. Austin, R. Cammi, C. Pomelli, J.W. Ochterski, R.L. Martin, K. Morokuma, V.G. Zakrzewski, G.A. Voth, P. Salvador, J.J. Dannenberg, S. Dapprich, A.D. Daniels, O. Farkas, J.B. Foresman, J.V. Ortiz, J. Cioslowski, D.J. Fox, Gaussian 09, Revision D.01, Gaussian, Inc., Wallingford, CT, 2013.

42 P.J. Hay, W.R. Wadt, J. Chem. Phys. 82 (1985) 299-310.

43 Gauss View 5.0.9 (Gaussian Inc., Wallingford, CT, USA) (2009).

44 A.E. Reed, R.B. Weinstock, F. Weinhold, J. Phys. Chem. 83 (1985) 735–746.

45 (a) R. Bauernschmitt, R. Ahlrichs, Chem. Phys. Lett. 256 (1996) 454–464; (b) R.E. Stratmann, G.E. Scuseria, M.J. Frisch, J. Chem. Phys. 109 (1998) 8218–8224; (c) M.E. Casida, C. Jamorski, K.C. Casida, D.R. Salahub, J. Chem. Phys. 108 (1998)

4439–4449.

46 (a) V. Barone, M. Cossi, J. Phys. Chem. 102 (1998) 1995–2001; (b) M. Cossi, V. Barone, J. Chem. Phys. 115 (2001) 4708–4717.

47 I.P. Tripathi, A. Kamal, M.K. Mishra, A. Dwivedi, R. Tripathi, C. Mishra and L. Shastri, Indian J. Appl. Res. 4 (2014) 66-69.

48 S. Al-Zuhair, A. Dowaidar, H. Kamal, J. Biochem. Tech. 2 (2010) 158-160.

49 P. Sudha, S.Z. Smita, Y.B. Shobha, R.K. Ameeta, BMC Compliment. Altern. Med. 11 (2011) 5.

50 A.K. Patel, R.N. Jadeja, H. Roy, R.N. Patel, S.K. Patel, R.J. Butcher, J. Mol. Struct. 1185 (2019) 341-350.

51 A. Ahmed, O.B. Chanu, A. Koch, R.A. Lal, J. Mol. Struct. 1029 (2012) 161–168.

52 Aziz Ahmed, Ram A. Lal, J. Mol. Struct. 1048 (2013) 321–330.

53 I. Syiemlieh, M. Asthana, S.D. Kurbah, R.A. Lal, Polyhedron 170 (2019) 202-216.

54 R.A. Lal, D. Basumatary, A.K. De, A. Kumar, Trans. Met. Chem. 32 (2007) 481-493.

55 S. Samanta, D. Ghosh, S. Mukhopadhyay, A. Endo, T.J.R. Weakley, M. Chaudhury, Inorg. Chem. 42 (2003) 1508-1517.

56 M.S. Nair, R.S. Joseyphus, Spectrochim Acta A 70 (2008) 749-753.

57 S.A. Sallam, Transition Met. Chem. 31 (2006) 46-45.

58 W.J. Geary, Coord. Chem. Rev. 7 (1971) 81-122.

59 T. Gosh, Transit. Met. Chem. 31 (2006) 560-565.

60 M.R. Maurya, A. Kumar, M. Ebel, D. Rehder, Inorg. Chem. 45 (2006) 5924–5937.

61 B. Mondal, T. Ghosh, M. Sutradhar, G. Mukherjee, M.G.B. Drew, T. Ghosh, Polyhedron 27 (2008) 2193–2201.

62 S.P. Perlepes, D. Nicholls, M.R. Harrison, Inorg. Chim. Acta. 102 (1985) 137-143.

63 S. Samanta, D. Ghosh, S. Mukhopadhyay, A. Endo, T.J.R. Weakley, M. Chaudhury, Inorg. Chem. 42 (2003) 1508−1517.

64 M.R. Maurya, A.A. Khan, A. Azam, S. Ranjan, N. Mondal, A. Kumar, F. Avecillae, J.C. Pessoa, Dalton Trans. 39 (2010) 1345–1360.

65 X. Li, M.S. Lah, V.L. Pecoraro, Inorg. Chem. 27 (1988) 4657-4664.

66 A.G.J. Ligtenbarg, A.L. Spek, R. Hage, B.L. Feringa, J. Chem. Soc., Dalton Trans.

(1999) 659-662.

67 M.R. Maurya, S. Khurana, C. Schulzke, D. Rehder, Eur. J. Inorg. Chem. 2001 (2001) 779-788.

68 N.R. Sangutha, S. Pall, Bull. Chem. Soc. Japn. 73 (2000) 357-363.

69 S.P. Dash, S. Majumder, A. Banerjee, M. Fernanda, N.N. Carvalho, P. Adao, J.C. Pessoa, K. Brzezinski, E. Garribba, H. Reuter, R. Dinda, Inorg. Chem. 55 (2016) 1165–1182.

70 I. Syiemlieh, M. Asthana, S.D. Kurbah, R.A. Lal, Polyhedron 170 (2019) 202–216.

71 A.A. Isse, A. Cennaro, E. Vianello, Electrochimica. Acta., 42 (1997) 2065-2071.

72 K. Bhattacharya, Sk Md TowsifAbtab, M.C. Majee, A. Endo, M. Chaudhury, Inorg. Chem. 53 (2014) 8287–8297.

73 T.K. Paine, T. Weyhermuller, L.D. Slep, F. Neese, E. Bill, E. Bothe, K. Wieghardt, P. Chaudhuri, Inorg. Chem. 43 (2004) 7324–7338.

74 M.A. Spackman, J.J. McKinnon, Cryst. Eng. Comm. 4 (2004) 378-392.

75 M.A. Spackman, P.G. Byrom, Chem. Phy. Lett. 267 (1997) 309.

76 J.J. McKinnon, A.S. Mitchell, M.A. Spackman, J. Eur. Chem. 4 (1998) 2136-2141.

77 J.J. McKinnon, M.A. Spackman, A.S. Mitchell, Acta Crystallogr. Sec. B. 60 (2004) 627-668.

78 A.L. Rohl, M. Moret, W. Kaminsky, K. Claborn, J.J. McKinnon, B. Kahr, Cryst. Growth Des. 8 (2008) 4517-4525.

79 A. Parkin, G. Barr, W. Dong, C.J. Gilmore, D. Jayatilaka, J.J. McKinnon, M.A. Spackman, C.C. Wilson, Cryst. Eng. Comm. 9 (2007) 648-652.

80 S.K. Wolff, D.J. Greenwood, J.J. McKinnon, D. Jayatilaka, M.A. Spackman, Crystal Explorer 2.0; University of Western Australia: Perth, Australia, 2007.

81 J.J. Koenderink, A.J.V. Doorn, Image Vision Comput. 10 (1992) 557-564.

82 P.K. Sasmel, A.K. Patre, A.R. Chakravarty, J. Inorg. Biochem. 102 (2008) 1463-1472.

83 R. Jawari, M. Hussian, M. Khalid, Inorg. Chim. Acta 486 (2019) 162-171.

84 S.K.S. Hazari, J. Kopf, D. Palit, S. Rakshit, D. Rehder, Inorg. Chim. Acta 362 (2009) 1343-1347.

85 B.S. Parajo´n-Costa, O.E. Piro, R. Pis-Diez, E.E. Castellano, A.C. Gonza´lez-Baro, Polyhedron 25 (2006) 2920-2928.

86 T. K. -Dobravc, A. Meden, F. Perdih, New J. Chem. 39 (2015) 4265-4277.

87 T. Koopmans, Physica 1 (1934) 104-113.

88 M.R. Maurya, B. Sarkar, F. Avecilla, I. Correia, Dalton Trans. 45 (2016) 17343-17364.

89 S. Mahajan, B. Singh, H.N. Sheikh, B.L. Kalsotra, Chem. Sci. Trans. 1 (2012) 23-34

90 B. Tiwari, I.P. Tripathi, S.S. Haribhusan, A.P. Dwivedi, R. Dubey, Int. J. Chem. Res. 2 (2011) 4239-4245.

91 G.R. Willsky, L-H Chi, M. Godzala III, P.J. Kostyniak, J.J. Smee, A.M. Trujillo, J.A. Alfano, W. Ding, Z. Hu, D.C. Crans, Coord. Chem. Rev. 255 (2011) 2258-2269.

92 S. Zahang, S.M. Kiren, Appl. Organomet. Chem. 5102 (2019) 11-12.

93 M.K. Bhat, B.S. Chodha, B.A. Kumar, G.S. Kaur, J. Gen. Micro-biol. 139 (1993) 2825-2832.

94 S. Bharathi, D. Mahendiran, R.S. Kumar, A.K. Rahiman, Chem. Select. 5 (2020) 6245-6254.

95 B. Kimmel, S.E. Inzncchi, Clin. Diabetes. 23 (2005) 64-76.

Published Paper from this chapter

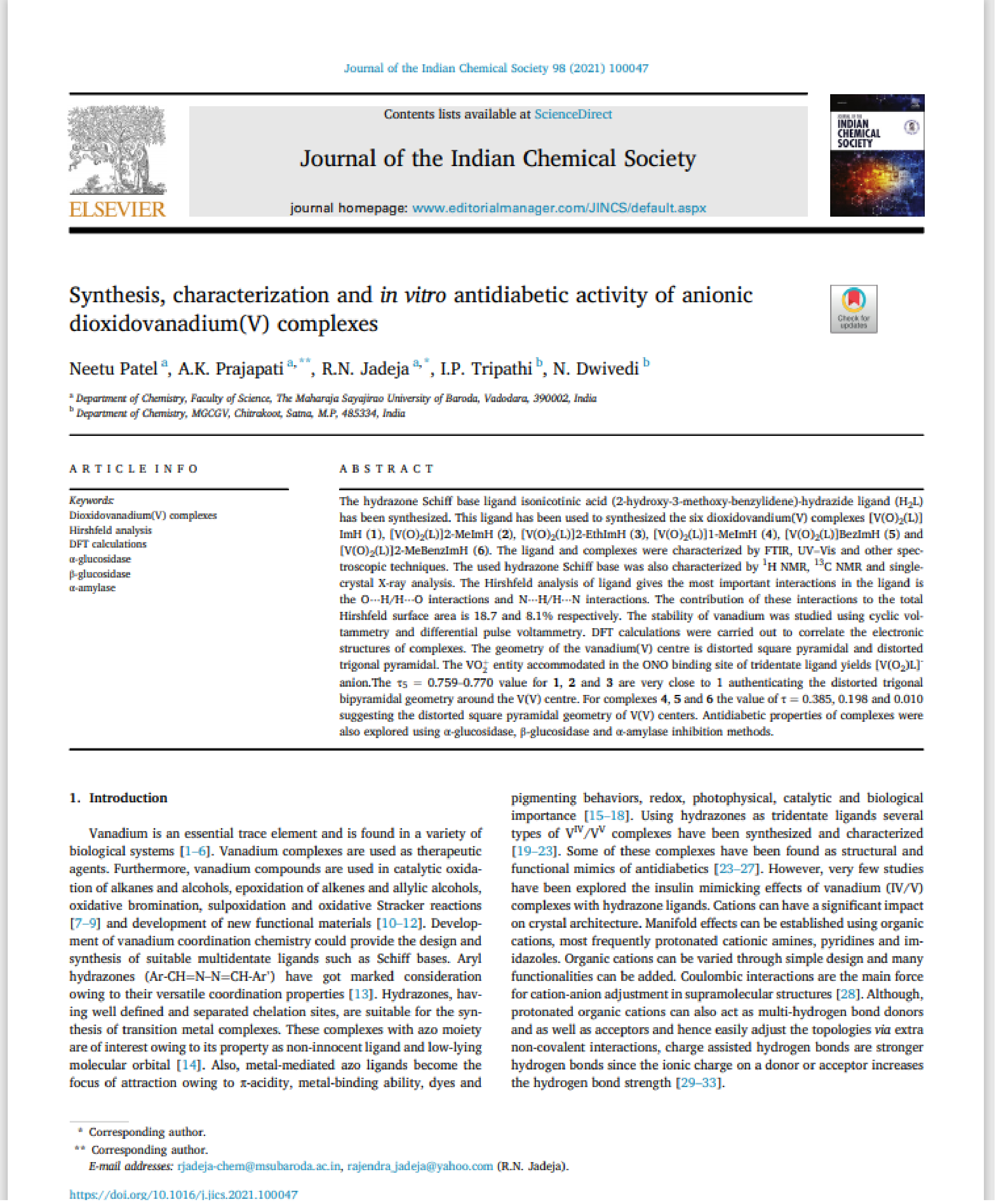

Journal of the Indian Chemical Society 98 (2021) 100047

Contents lists available at ScienceDirect

Journal of the Indian Chemical Society

journal homepage: www.editorialmanager.com/JINCS/default.aspx

Synthesis, characterization and *in vitro* antidiabetic activity of anionic dioxidovanadium(V) complexes

Neetu Patel [a], A.K. Prajapati [a, **], R.N. Jadeja [a, *], I.P. Tripathi [b], N. Dwivedi [b]

[a] *Department of Chemistry, Faculty of Science, The Maharaja Sayajirao University of Baroda, Vadodara, 390002, India*
[b] *Department of Chemistry, MGCGV, Chitrakoot, Satna, M.P, 485334, India*

ARTICLE INFO

Keywords:
Dioxidovanadium(V) complexes
Hirshfeld analysis
DFT calculations
α-glucosidase
β-glucosidase
α-amylase

ABSTRACT

The hydrazone Schiff base ligand isonicotinic acid (2-hydroxy-3-methoxy-benzylidene)-hydrazide ligand (H_2L) has been synthesized. This ligand has been used to synthesized the six dioxidovandium(V) complexes $[V(O)_2(L)]ImH$ (**1**), $[V(O)_2(L)]$2-MeImH (**2**), $[V(O)_2(L)]$2-EthImH (**3**), $[V(O)_2(L)]$1-MeImH (**4**), $[V(O)_2(L)]$BezImH (**5**) and $[V(O)_2(L)]$2-MeBenzImH (**6**). The ligand and complexes were characterized by FTIR, UV–Vis and other spectroscopic techniques. The used hydrazone Schiff base was also characterized by ^1H NMR, ^{13}C NMR and single-crystal X-ray analysis. The Hirshfeld analysis of ligand gives the most important interactions in the ligand is the O···H/H···O interactions and N···H/H···N interactions. The contribution of these interactions to the total Hirshfeld surface area is 18.7 and 8.1% respectively. The stability of vanadium was studied using cyclic voltammetry and differential pulse voltammetry. DFT calculations were carried out to correlate the electronic structures of complexes. The geometry of the vanadium(V) centre is distorted square pyramidal and distorted trigonal pyramidal. The VO_2^+ entity accommodated in the ONO binding site of tridentate ligand yields $[V(O_2)L]^-$ anion.The $\tau_5 = 0.759–0.770$ value for **1**, **2** and **3** are very close to 1 authenticating the distorted trigonal bipyramidal geometry around the V(V) centre. For complexes **4**, **5** and **6** the value of $\tau = 0.385$, 0.198 and 0.010 suggesting the distorted square pyramidal geometry of V(V) centers. Antidiabetic properties of complexes were also explored using α-glucosidase, β-glucosidase and α-amylase inhibition methods.

1. Introduction

Vanadium is an essential trace element and is found in a variety of biological systems [1–6]. Vanadium complexes are used as therapeutic agents. Furthermore, vanadium compounds are used in catalytic oxidation of alkanes and alcohols, epoxidation of alkenes and allylic alcohols, oxidative bromination, sulpoxidation and oxidative Stracker reactions [7–9] and development of new functional materials [10–12]. Development of vanadium coordination chemistry could provide the design and synthesis of suitable multidentate ligands such as Schiff bases. Aryl hydrazones (Ar-CH=N–N=CH-Ar') have got marked consideration owing to their versatile coordination properties [13]. Hydrazones, having well defined and separated chelation sites, are suitable for the synthesis of transition metal complexes. These complexes with azo moiety are of interest owing to its property as non-innocent ligand and low-lying molecular orbital [14]. Also, metal-mediated azo ligands become the focus of attraction owing to π-acidity, metal-binding ability, dyes and pigmenting behaviors, redox, photophysical, catalytic and biological importance [15–18]. Using hydrazones as tridentate ligands several types of V^{IV}/V^V complexes have been synthesized and characterized [19–23]. Some of these complexes have been found as structural and functional mimics of antidiabetics [23–27]. However, very few studies have been explored the insulin mimicking effects of vanadium (IV/V) complexes with hydrazone ligands. Cations can have a significant impact on crystal architecture. Manifold effects can be established using organic cations, most frequently protonated cationic amines, pyridines and imidazoles. Organic cations can be varied through simple design and many functionalities can be added. Coulombic interactions are the main force for cation-anion adjustment in supramolecular structures [28]. Although, protonated organic cations can also act as multi-hydrogen bond donors and as well as acceptors and hence easily adjust the topologies *via* extra non-covalent interactions, charge assisted hydrogen bonds are stronger hydrogen bonds since the ionic charge on a donor or acceptor increases the hydrogen bond strength [29–33].

---

* Corresponding author.
** Corresponding author.
E-mail addresses: rjadeja-chem@msubaroda.ac.in, rajendra_jadeja@yahoo.com (R.N. Jadeja).

https://doi.org/10.1016/j.jics.2021.100047